# Axisymmetry in protoplanetary nebulae: using imaging polarimetry to investigate envelope structure

T. M. Gledhill,[★] A. Chrysostomou, J. H. Hough and J. A. Yates

*Department of Physical Sciences, University of Hertfordshire, College Lane, Hatfield, Hertfordshire AL10 9AB*

**ABSTRACT**

We use ground-based imaging polarimetry to detect and image the dusty circumstellar envelopes of a sample of protoplanetary nebulae (PPNe) at near-infrared wavelengths. This technique allows the scattered light from the faint envelope to be separated from the glare of the bright central star, and is particularly well suited to this class of object. We detect extended (up to 9-arcsec diameter) circumstellar envelopes around 15 out of 16 sources with a range of morphologies including bipolars and shells. The distribution of scattered light in combination with its polarization (up to 40 per cent) provides unambiguous evidence for axisymmetry in 14 objects, showing this to be a common trait of PPNe. We suggest that the range of observed envelope morphologies results from the development of an axisymmetric dust distribution during the superwind phase at the end of the AGB. We identify shells seen in polarized light with scattering from these superwind dust distributions, which allows us to provide constraints on the duration of the superwind phase. In one object (IRAS 19475+3119) the circumstellar envelope has a two-armed spiral structure, which we suggest results from the interaction of the mass-losing star with a binary companion.

**Key words:** polarization – scattering – stars: AGB and post-AGB – circumstellar matter.

## 1 INTRODUCTION

Protoplanetary nebulae (PPNe) represent a transition phase in the evolution of low- and intermediate-mass stars between the asymptotic giant branch (AGB) and the planetary nebula (PN) phases (Kwok 1993). During its AGB lifetime, a star undergoes periods of intense mass-loss, with mass-loss rates of up to $10^{-5}\,M_\odot\,yr^{-1}$ (Loup et al. 1993), resulting in the formation of a circumstellar envelope (CSE) of dust and gas. After mass-loss ceases at the end of the AGB, the envelope continues to expand and to disperse during the next $\sim 10^3$ yr of evolution as a PPN, and subsequently as a PN.

By studying the CSEs of PPNe, much can be learned about the mass-loss process during the AGB phase, since the envelope structure is a cumulative record of the mass-loss history. One particularly striking development is the emergence of axisymmetry in the CSE, as observed, for example, in bipolar PPNe such as AFGL 2688 (Sahai et al. 1998a,b), IRAS 17150−3224 (Kwok, Su & Hrivnak 1998) and IRAS 17441−2445 (Su et al. 1998). It is currently thought that a dramatic increase in mass-loss occurs at the end of the AGB (the 'superwind' phase), and that this may be responsible for initiating the shift from spherical to axisymmetric structure in the CSE, if the wind is intrinsically axisymmetric (e.g. Meixner et al. 1997). The result is the ejection of a superwind

shell of gas and dust which has a flattened density distribution, being more equatorially concentrated, which can then collimate any further outflow along the polar axis.

Until recently, however, resolved images of CSEs existed for only a few large, bipolar PPNe, compared with a list of PPNe candidates numbering over 100 (Volk & Kwok 1989), and so this model has not been well tested. In many PPNe, the dust shell has thinned to the extent that the central star is visible at optical and near-infrared (NIR) wavelengths which can make them very difficult to resolve from the ground. If the nebulosity is less than $\sim 5$ arcsec in extent, then, with a 4-m class telescope, the CSE is likely to be hidden by the extended wings of the point spread function (PSF) of the bright central star, so that the PPN appears star-like from the ground. To glean any information on the CSE structure requires deconvolution or PSF subtraction, which can be difficult given the huge difference in the brightness of the central star and the faint CSE (e.g. Hrivnak et al. 1999a). By moving to space-based observations, the problems caused by the scattering of light from bright central stars in the Earth's atmosphere are overcome, allowing the possibility of resolving the CSEs of these PPNe in more detail. Ueta, Meixner & Bobrowsky (2000) have undertaken an optical imaging survey of PPNe using the Wide Field and Planetary Camera 2 (WFPC2) on the *HST*, and detect extended nebulosity in 21 of their 27 targets.

Ground-based imaging polarimetry provides an alternative technique, which is particularly well suited to resolving structure

[★] E-mail: T.Gledhill@star.herts.ac.uk

**Table 1.** A summary of the observations, indicating the filters used, the date of the observation, and the exposure and total integration times in seconds. The full-width half-maxima (FWHM) of the targets and nearby reference stars, where available, are given for those sources that appear point source-like in total flux (all except 20028+3910).

| IRAS ID | RA (J2000) | Dec. (J2000) | Filter | Date | Exposure | Integration | FWHM(target) | FWHM(ref) |
|---|---|---|---|---|---|---|---|---|
| 17106−3046 | 17 13 51.7 | −30 49 40 | *J* | 26/6/99 | 4 | 432 | 0.98 | 0.91 |
|  |  |  | *K* | 26/6/99 | 1 | 432 | 0.74 | 0.68 |
| 17245−3951 | 17 28 04.6 | −39 53 43 | *J* | 26/6/99 | 10 | 720 | 1.16 | 0.95 |
| 17436+5003 | 17 44 54.9 | +50 02 38 | *J* | 5/5/98 | 0.25 | 400 | 0.57 | − |
|  |  |  | *K* | 5/5/98 | 0.25 | 300 | 0.50 | 0.47 |
| 18095+2704 | 18 11 30.6 | +27 05 14 | *J* | 5/5/98 | 3 | 540 | 1.01 | 0.80 |
|  |  |  | *K* | 7/5/98 | 0.15 | 180 | 0.51 | 0.32 |
| 18184−1623 | 18 21 19.5 | −16 22 26 | *J* | 26/6/99 | 0.072 | 518 | 0.72 | 0.64 |
| 19114+0002 | 19 13 58.7 | +00 07 31 | *J* | 5/5/98 | 0.12 | 360 | 0.78 | 0.81 |
|  |  |  | *H* | 8/5/98 | 0.12 | 240 | 0.85 | 0.69 |
|  |  |  | *K* | 6/5/98 | 0.12 | 360 | 0.96 | 0.91 |
| 19454+2920 | 19 47 24.3 | +29 28 12 | *J* | 7/5/98 | 10 | 400 | 0.64 | 0.61 |
|  |  |  | *K* | 8/5/98 | 2 | 400 | 0.55 | 0.57 |
| 19475+3119 | 19 49 29.4 | +31 27 15 | *J* | 7/5/98 | 0.5 | 200 | 0.60 | 0.56 |
|  |  |  | *K* | 8/5/98 | 0.4 | 320 | 0.60 | 0.57 |
| 19477+2401 | 19 49 54.5 | +24 08 51 | *J* | 7/5/98 | 20 | 400 | 0.50 | 0.50 |
| 19500−1709 | 19 52 53.5 | −17 01 50 | *J* | 7/5/98 | 0.5 | 200 | 0.90 | 0.90 |
|  |  |  | *K* | 6/5/98 | 0.3 | 240 | 0.82 | − |
| 20000+3239 | 20 01 59.5 | +32 47 32 | *J* | 6/5/98 | 1 | 200 | 1.00 | 0.94 |
|  |  |  | *K* | 7/5/98 | 0.12 | 240 | 0.49 | 0.50 |
| 20028+3910 | 20 04 35.0 | +39 18 38 | *J* | 7/5/98 | 20 | 800 |  |  |
|  |  |  | *K* | 6/5/98 | 5 | 400 |  |  |
| 20056+1834 | 20 07 54.8 | +18 42 57 | *J* | 5/5/98 | 3 | 504 | 0.67 | 0.61 |
|  |  |  | *H* | 8/5/98 | 1 | 400 | 0.61 | 0.68 |
| 21027+5309 | 21 04 14.9 | +53 21 03 | *J* | 8/5/98 | 3 | 360 | 0.73 | 0.73 |
|  |  |  | *H* | 8/5/98 | 0.5 | 400 | 0.68 | 0.68 |
| 22223+4327 | 22 24 30.7 | +43 43 03 | *J* | 26/6/99 | 0.5 | 680 | 0.72 | 0.72 |
| 22272+5435 | 22 29 10.2 | +54 51 04 | *J* | 26/6/99 | 0.072 | 461 | 0.80 | 0.72 |

in the CSEs of PPNe when they are associated with bright central stars. Since PPNe are seen by scattered light in the optical and NIR, they are expected to be linearly polarized at these wavelengths. On the other hand, the stellar PSF, which is formed by scattering through tiny angles in the atmosphere, is effectively unpolarized. Imaging polarimetry provides the means to separate one from the other, so that in polarized light the central star effectively disappears, revealing the faint CSE. In this paper we use NIR imaging polarimetry to detect CSEs in a sample of 16 PPNe candidates and to image their structure.

## 2    EXPERIMENTAL DETAILS

### 2.1    Target list

We have selected targets from the literature which have properties typical of PPNe and which appear in previously published lists of PPNe candidates (e.g. Kwok 1993; Meixner et al. 1999). Most have a mid-infrared (MIR) excess typical of emission from a cool dusty CSE, and a double-peaked SED indicating that the envelope is detached from the star. We have not selected the targets on the grounds of morphology, and indeed all appear point source-like in previously published ground-based imaging. Despite their common properties, it is likely that at least one of our targets, IRAS 18184−1623, is not a PPN, and there is debate over the status of another (IRAS 19114+0002). Nevertheless, they are retained in the sample. An effective cut-off of $K > 4.2$ was imposed by the NIR detector, below which targets were too bright to observe without saturation. The target list is shown in Table 1. The coordinates given are those found in the SIMBAD data base.

### 2.2    Observations

Observations were made at the 3.8-m United Kingdom Infrared Telescope (UKIRT) on Mauna Kea, Hawaii, using the facility infrared camera IRCAM3. The $256 \times 256$ element InSb detector is sensitive between 1 and 5 $\mu$m, and was used in conjunction with *J*, *H* and *K* broad-band filters. A warm $2\times$ magnifying lens was inserted in front of the cryostat window to provide a scale of 0.143 arcsec per pixel with a field of view of approximately 40 arcsec.

Dual-beam imaging polarimetry was obtained using an upstream rotating half-wave-plate assembly (IRPOL2), along with a lithium niobate Wollaston prism located in a filter wheel in the detector cryostat. An aperture mask mounted at a focal plane between IRPOL2 and IRCAM3 allows two $40 \times 10$ arcsec$^2$ sky segments to be imaged side by side on the detector in orthogonal polarization states with minimum overlap. This standard configuration for dual-beam polarimetry is described in more detail by Berry & Gledhill (1999).

The data presented in this paper were obtained on two separate observing runs, in 1998 May and in 1999 June. The 1998 run consisted of four consecutive second-half shifts on May 5, 6, 7 and 8, and the run in 1999 consisted of a single night on June 26. Conditions on 1998 May 5, 6 and 8 were less than ideal, with varying degrees of cloud cover. The nights of 1998 May 7 and 1999 June 26 were clear and photometric. Image correction was provided by a tip-tilt secondary, which resulted in image quality consistently better than 1 arcsec and frequently better than 0.5 arcsec (FWHM). Although an identical instrument configuration and observing method were used on both runs, an upgrade to the telescope secondary mirror resulted in a significantly improved PSF in the 1999 June data.

A total of 16 targets were observed, and details are given in Table 1. The duration of exposures was chosen so as to operate the detector within its linear response range. Where this was not possible (due to the brightness of the target), a known linearity correction has been applied. For exposure times of 1 s and greater, a non-destructive readout mode was used (ND+STARE). For shorter exposures, a direct readout mode (STARE) was used. For extremely bright targets ($K < 5$) requiring exposure times of less than 120 ms, a fast readout mode was also employed. In all cases the total integration time includes measurements at several positions on the array (jitters) to minimize the effect of detector defects. Each jitter position was observed at four orientations of the half-wave plate (separated by $22°.5$) to obtain linear polarimetry, and these images are in turn made up of co-added exposures to increase the signal-to-noise ratio.

### 2.3 Data reduction

After dark subtraction and flat-fielding, all target data were reduced in an identical manner using the dual-beam imaging polarimetry package POLPACK (Berry & Gledhill 1999). The software aligns component images to a common coordinate system and, after correction for instrumental polarization, combines the data to form resultant $I$, $Q$ and $U$ Stokes images, from which the other polarized quantities are obtained. Variance estimates from the raw data are propagated through the calculation to provide errors on the final $I$, $Q$ and $U$ images, and on the derived polarized quantities $P$ (degree of polarization) and $I_\mathrm{p}$ (polarized flux). In all cases the linear polarization shown has been debiased using the variance on the $Q$ and $U$ Stokes intensities to account for the non-symmetric noise statistics produced when adding and squaring $Q$ and $U$.

## 3  RESULTS

### 3.1  Format of results

In this section we present our imaging polarimetry results, which

are displayed in the same format for each target. In each case we show grey-scale images of total flux superimposed with a polarization vector map. The polarization vectors are oriented parallel to the E vector, with their length proportional to the degree of linear polarization, as indicated by the scale vector on each diagram. Unless otherwise indicated, each polarization measurement (vector) corresponds to an average over a $3 \times 3$ pixel (0.43 arcsec square) bin. In addition, a $2\sigma$ cut has been imposed so that only measurements with an error in the degree of polarization less than one-half of the polarization are plotted; this has the effect of excluding noisy measurements in low signal-to-noise regions, such as on the sky.

We also show grey-scale images of polarized flux, $I_\mathrm{p}$ for each object. Contours are superimposed on the grey-scale images where these serve to highlight structure in the polarized flux. In these cases the contours are spaced logarithmically at intervals of 1.0 mag, unless otherwise stated. Since conditions were non-photometric for most of the run, the data have not been flux-calibrated, and the contour levels are therefore in arbitrary units. The lack of photometric calibration or conditions in no way affects the polarimetric results, since dual beam polarimetry eliminates the effects of varying sky conditions.

We summarize the results for each object in Table 2 in Section 3.3, which includes details of angular extent, morphology and degrees of polarization (see Section 3.1.1). Nearly all of our targets have bright, point source-like cores in total flux, and in Table 1 we list the full-width half-maxima (FWHM) of the cores. We also list the FWHM of nearby PSF comparison stars to indicate the seeing conditions at the time of the observations. Objects are referred to by their *IRAS* identifiers. Position angles (PAs) are quoted east of north. The labels N, E, S and W, and combinations thereof, are used to denote compass points.

### 3.1.1  A note on the degree of polarization

In the majority of our targets, the central star is visible in the NIR and dominates the total flux. Although the polarized flux images

**Table 2.** A summary of the polarimetric results for the 16 PPNe in our survey. We categorize the objects according to their appearance in polarized flux as *shell*, *bipolar* or *core-dominated*, as described in Section 3.3. The important dimensions are given along with the peak degrees of polarization (Section 3.1.1).

| Target | Category[a] | Pol. Map[b] | Polarized Flux[c] | Size ($''$)[d] | PA ($°$)[e] | Maximum Polarization (%)[f] |
|---|---|---|---|---|---|---|
| 17436+5003 | Shell | CS | Elongated Shell + Halo | $5.7 \times 3.6$ | 10 | $P_J = 20.2 \pm 2.2$  $P_K = 20.0 \pm 4.4$ |
| 19114+0002 | Shell | CS | Round Shell + Halo | $9.0 \times 9.0$ | – | $P_J = 28.8 \pm 4.4$  $P_H = 27.1 \pm 2.9$  $P_K = 25.5 \pm 4.9$ |
| 19475+3119 | Shell | CS | Point Symm. Shell + Halo | $4.9 \times 3.4$ | 145 | $P_J = 20.6 \pm 4.6$  $P_K = 11.3 \pm 2.5$ |
| 22272+5435 | Shell | CS | Elongated Shell + Halo | $4.0 \times 2.9$ | 125 | $P_J = 18.9 \pm 1.4$ |
| 22223+4327 | Shell/Bipolar | CS/EL | Shell + Bipolar | 2.3 (shell) | 127 (bip) | |
| 17106−3046 | Bipolar | EL | Bipolar | $3.2 \times 2.4$ | 10 | $P_J = 13.0 \pm 4.8$  $P_K = 6.5 \pm 0.8$ |
| 17245−3951 | Bipolar | AL/EL | Bipolar | $2.9 \times 1.6$ | 12 | $P_J = 20.3 \pm 1.0$ |
| 18095+2704 | Bipolar | EL/AL | Bipolar | $2.7 \times 2.3$ | 115 | $P_J = 2.4 \pm 0.8$  $P_K = 2.4 \pm 0.3$ |
| 19477+2401 | Bipolar | EL/AL | Bipolar | $2.1 \times 0.9$ | 30 | $P_J = 17.0 \pm 3.8$ |
| 19500−1709 | Bipolar | EL/AL | Bipolar | $3.6 \times 2.2$ | 100 | $P_J = 5.7 \pm 1.1$  $P_K = 6.1 \pm 2.1$ |
| 20000+3239 | Bipolar | EL/AL | Bipolar | $3.7 \times 3.3$ | 36 | $P_J = 6.1 \pm 1.5$  $P_K = 3.4 \pm 0.4$ |
| 18184−1623 | Core | AL | Point Source | – | – | $P_J = 2.4 \pm 0.6$ |
| 20028+3910 | Core | AL | Elongated Halo | $4.4 \times 3.3$ | 153 | $P_J = 34.0 \pm 2.8$  $P_K = 41.7 \pm 12.5$ |
| 20056+1834 | Core | AL | Point Source | – | – | $P_J = 14.2 \pm 6.1$  $P_H = 7.4 \pm 1.9$ |
| 21027+5309 | Core | AL | Point Source | – | – | $P_J = 17.6 \pm 3.1$  $P_H = 6.5 \pm 2.8$ |
| 19454+2920 | Unpolarized | – | – | – | – | – |

[a] the CSE category as defined in Section 3.3.
[b] the type of polarization map; CS (centrosymmetric), EL (elliptical), AL (aligned) or a combination, as defined in Section 3.3.
[c] the CSE morphology in polarized flux.
[d] the extent of the CSE in our *J*-band polarized flux images. For objects in the *Shell* category this is the major × minor axis of the halo. For *Bipolar* objects the major × minor axes of the bipolar are given. For *Core* objects, only 20028+3910 appears elongated, and the major × minor axes of the halo are given.
[e] The position angle (east of north) of the major axis, as defined by the polarized flux image.
[f] The maximum polarization in each waveband after application of various cuts (see Section 3.1.1). Note that the errors appear large in some cases because the largest polarizations often occur in the outer regions of the nebulosity where the signal-to-noise ratio is low.

correctly represent the intensity in scattered light from the CSE, the *degree* of polarization will be diluted by the superimposed unpolarized light from the extended PSF of the star. In order to calculate the true degree of polarization of the scattered light, the PSF of the star must be removed to reveal a total-flux image of the nebulosity. Even with a perfect PSF calibration, a PSF subtraction or deconvolution is likely to be only partially successful due to the huge dynamic range involved and the compact nature of the scattering region (i.e., the CSE lies within the wings of the PSF). In practice, we do not have suitable PSF calibrators for several targets and, given the non-photometric conditions throughout much of the run, we have not attempted to correct for the unpolarized light. The degrees of polarization ($P$) quoted throughout the paper are, therefore, lower limits on the actual degree of polarization. Where we quote values for the 'maximum polarization' in each object, this is the maximum degree of polarization detected, using 0.43 arcsec square ($3 \times 3$ pixel) bins, after applying the $2\sigma$ cut mentioned above.

### 3.2 Individual objects

#### 3.2.1 IRAS 17106−3046

We show *J*- and *K*-band observations of 17106−3046 in Fig. 1. In the *J* band the object appears extended and slightly elongated in the NW−SE direction. Taking a contour level of 5 times the rms fluctuation in the sky background ($5\sigma_{sky}$) gives an extent of $3.0 \times 2.6$ arcsec$^2$. This is in agreement with Hrivnak et al. (1999a), who found that 17106−3046 has an angular size of 2.9 arcsec in the *V* band. However, we do not see evidence for elongation of the bright core in our *J* and *K* data, apparent in their *V* data. Although the core of the surface brightness image is quite centrally peaked in both wavebands (Table 1), the *J*-band image shows evidence for a diffuse halo that extends to the NE of 17106−3046 and encompasses the faint source found there. This source appears to be a faint star and may be in association with 17106−3046. The halo is not apparent in our *K*-band image.

The linear polarization maps shown in Fig. 1 demonstrate that 17106−3046 possesses an extended circumstellar envelope which is seen by scattered light, forming a reflection nebula. The pattern of polarization vectors is typical of illumination from a central source, which is in keeping with our observation that this source is centrally peaked at infrared wavelengths. However, the pattern is not centrosymmetric, as would be expected for single scattering in an optically thin medium with a point source illuminator, and shows vectors oriented preferentially along a PA of 101°. This vector pattern is typical of scattering in an axisymmetric geometry with the axis at PA 10°, perpendicular to the vector orientation.

The polarized flux images trace the regions in which scattering is occurring and are clearly bipolar. Contours are overlaid on the images to show detail in the central regions and reveal a bipolar structure oriented at PA 10°, perpendicular to the elongation in the total-flux image. The maximum extent of the object as defined by the polarized flux is $3.2 \times 2.4$ arcsec$^2$. The bipolar nature of the polarized flux distribution is further highlighted by the 'pinch' in the contours perpendicular to the bipolar axis in the equatorial
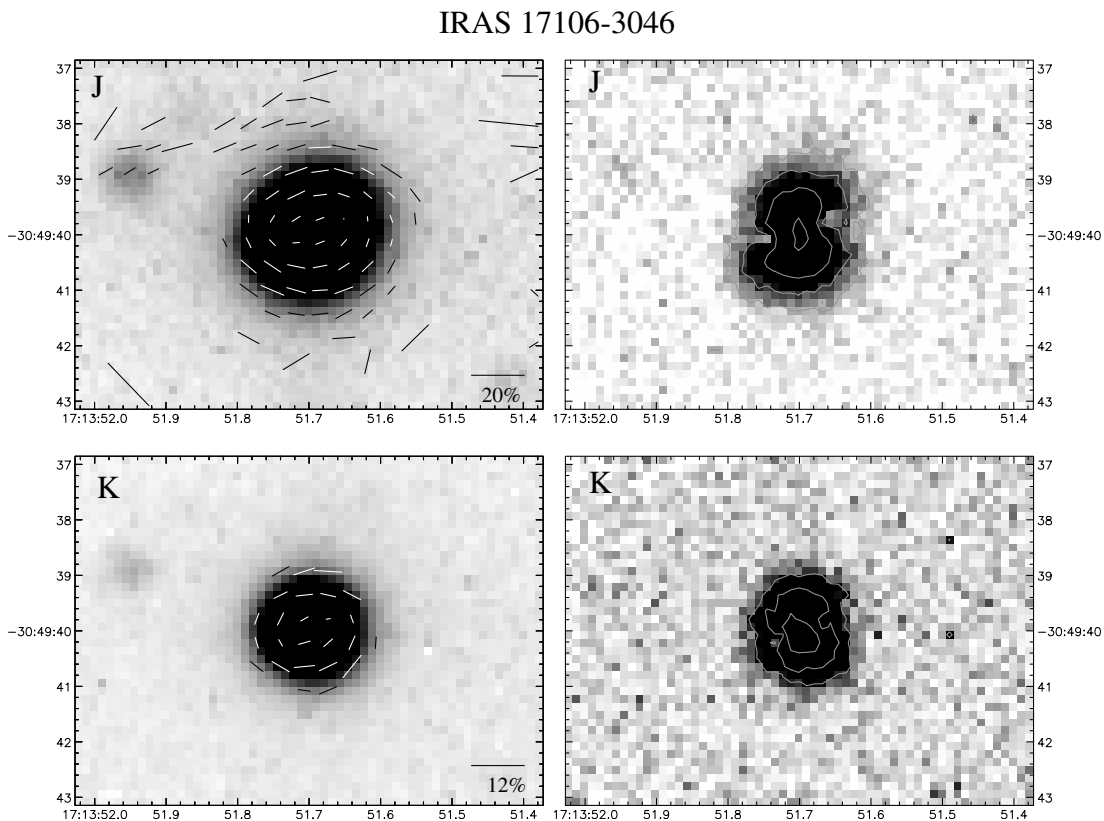
IRAS 17106-3046



**Figure 1.** Polarimetric observations of IRAS 17106−3046 in the *J* (upper) and *K* (lower) bands. The left-hand panels show grey-scale images of total flux superimposed with linear polarization maps (as described in Section 3.1.1). The right-hand panels show grey-scale images of polarized flux with selected contours superimposed to highlight structure in the image. The contours are spaced logarithmically at intervals of 1 mag. The coordinate system is centred on the peak of the total-flux image, using the coordinates in Table 1, and is plotted with Right Ascension and Declination (J2000) along the horizontal and vertical axes.
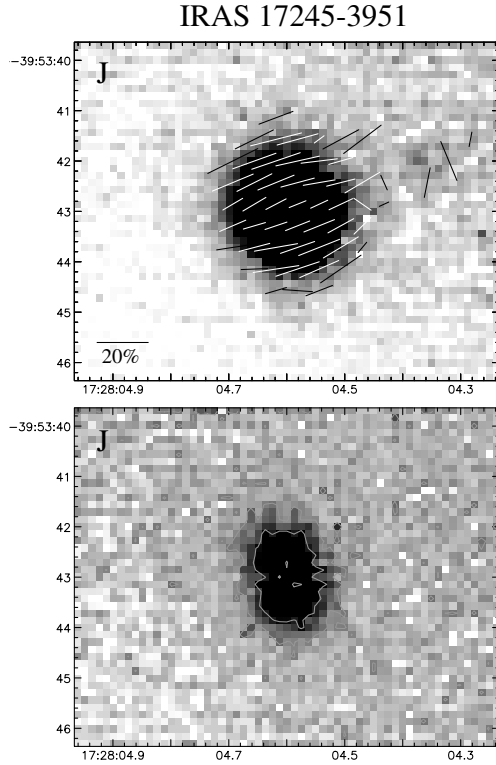
## IRAS 17245-3951



**Figure 2.** Polarimetric observations of IRAS 17245−3951 in the *J* band. The upper panel shows a grey-scale image of total flux superimposed with a linear polarization map (as described in Section 3.1.1). The lower panel shows a grey-scale image of polarized flux, with contours superimposed to highlight structure in the image. Other details are as in Fig. 1.

region. At fainter levels, there is evidence for an extension in polarized flux to the NW of the nebula. This may indicate a realignment of the bipolar axis from a PA of 10° in the central regions to a more NW direction in the outer regions. In the *K* band, the bipolarity in polarized flux is still clear, although the nebula is more compact. This could be due to our lower detection threshold in the *K* band, but is also consistent with a scattering cross-section that falls off rapidly with increasing wavelength, as would be typical of submicron dust particles at NIR wavelengths.

We also note that there is some evidence for meaningful polarization in the faint halo to the NE of 17106−3046, extending to the second faint source. However, the polarization vectors do not conclusively indicate that this region is illuminated by 17106−3046.

### 3.2.2   *IRAS 17245−3951*

*J*-band observations of 17245−3951 are shown in Fig. 2. The grey-scale total-flux image appears slightly elongated in a direction just east of north, suggesting that 17245−3951 is a diffuse source at the *J* band, and that we are not seeing through to the star. Taking a contour level at $5\sigma_{\text{sky}}$, the extent of the object in the *J* band is $3.5 \times 3.1 \, \text{arcsec}^2$.

The polarization vectors are aligned at a PA of 103° rather than being centrosymmetric. Such aligned vector patterns are seen frequently in observations of embedded young stellar objects (YSOs), and are typical of scattering in an optically thick and axially symmetric geometry, such as a dense circumstellar disc or torus (e.g. Lucas & Roche 1998). Along this axis away from the centre, the curvature in the vector pattern indicates that more optically thin scattering is occurring here, such as would be expected in the lobes of a bipolar nebula.
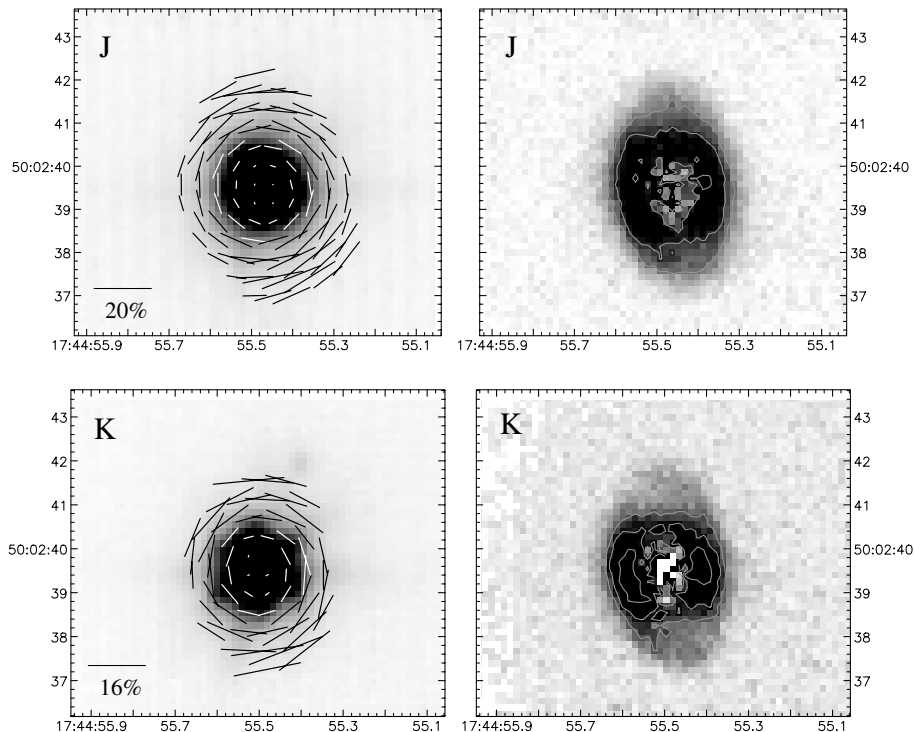
## IRAS 17436+5003



**Figure 3.** Polarimetric observations of IRAS 17436+5003 in the *J* and *K* bands. Details as for Fig. 1.

The bipolar nature of this object is confirmed by the polarized flux image shown in Fig. 2. The bipolar axis is oriented at PA 12°, aligned with the elongation in the total flux and perpendicular to the polarization vectors. This object is therefore a bipolar reflection nebula illuminated by an embedded source which is not directly visible in the *J* band. The extent of the object in polarized flux is $2.9 \times 1.6\,\mathrm{arcsec}^2$.

Recent WFPC2 imaging by Hrivnak, Kwok & Su (1999b) shows that $17245-3951$ is a bipolar nebula at optical wavelengths. They find a well-defined dark lane hiding the source and separating two lobes of nebulosity. They quote an orientation on the sky of 11° and an overall size (including the faint halo) of $2.8 \times 2.1\,\mathrm{arcsec}^2$. These results agree closely with ours, suggesting that the morphology is very similar in the optical and *J* bands.

### 3.2.3   IRAS 17436+5003

In Fig. 3 we show *J*- and *K*-band observations of $17436+5003$. The total-flux images show no evidence for extended emission, suggesting that the star is directly seen. Although the direct images show only a point-like structure, the linear polarimetry reveals that $17436+5003$ does have an extended envelope and that this is seen by scattered light. High degrees of polarization are evident in both *J* and *K* bands forming an almost perfect centrosymmetric pattern, indicating scattering in an optically thin medium with a point source illuminator. The similarity of the polarimetry in the *J* and *K* bands (Table 2) implies that (i) small dust grains ($<0.1\,\mu\mathrm{m}$) are responsible for scattering the light and

(ii) the scattering geometry is very similar at *J* and *K* (i.e., there are no optical depth effects). The polarization pattern extends more in the N–S direction than in the E–W direction, suggesting that the reflection nebula is slightly elongated. In addition, the polarizations in the N–S direction are larger by up to a factor of 2 than those in the E–W direction, which could be interpreted as a narrowing in the range of scattering angles (along the line of sight) in the N–S direction. These subtle deviations from centrosymmetry imply that the scattering geometry is not spherically symmetric and instead possesses an element of axisymmetry. The degrees of linear polarization towards the core of $17436+5003$ decrease to very small values. These regions are heavily affected by the bright PSF from the star, so that any light polarized by scattering in the stellar envelope will be greatly diluted by the unpolarized light from the star itself. The polarized flux images shown in Fig. 3 bear no resemblance to the direct images and reveal the true nature of the scattering envelope surrounding this star. Most of the scattering occurs in two bright arcs on either side of the source, with a fainter elliptical halo of scattered light extending to the N and S. The core of the polarized flux image is contaminated by residuals from the bright stellar PSF, but sufficient information remains to reveal clearly the shell-like structure of the scattered light.

We suggest a geometry for $17436+5003$, consisting of an ellipsoidal dusty envelope surrounding the star. Scattering of light within this envelope results in the faint halo seen in polarized flux. The bright arcs then result from limb-brightening as light is scattered within a shell-like density enhancement embedded within the envelope. The thickness of the shell is difficult to
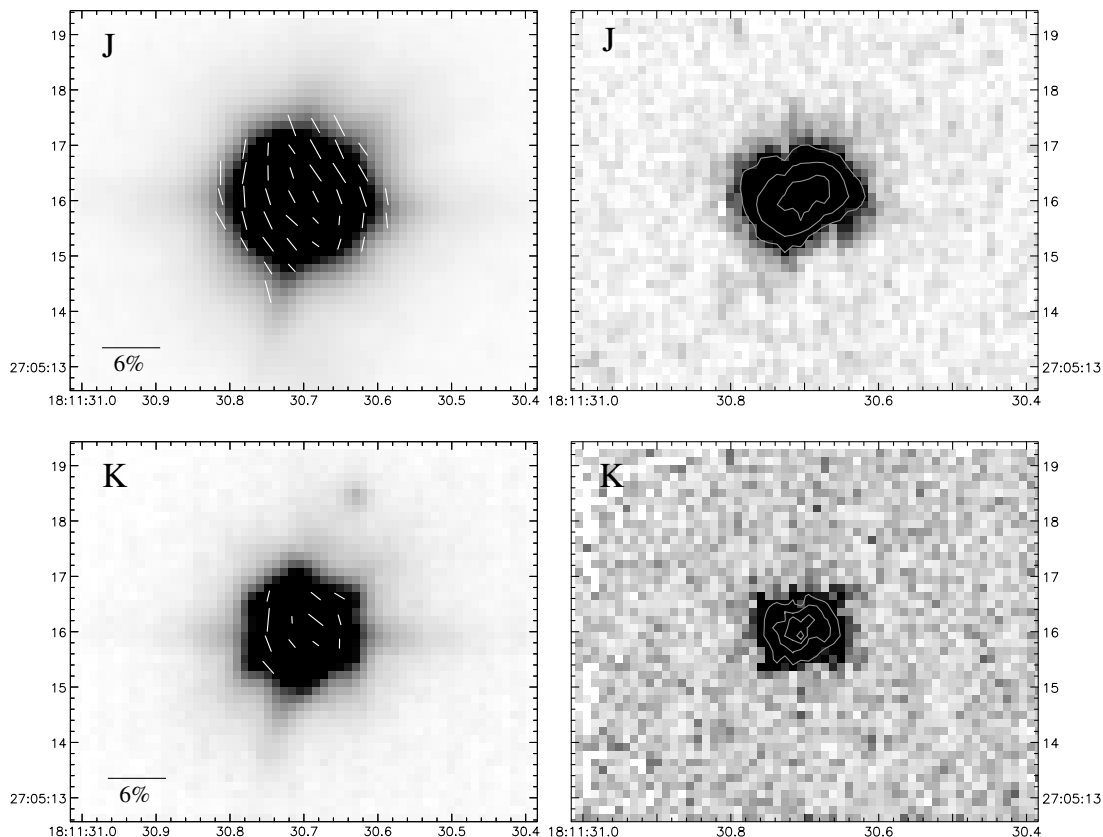


Figure 4. Polarimetric observations of IRAS 18095+2704 in the *J* and *K* bands. Details as for Fig. 1.

assess quantitatively, but a cut through the arcs in an E–W direction gives a FWHM of 0.86 arcsec in the *J* band. In the *K* band the arcs appear shorter and thicker. The shell is thinner in the polar regions, along the major axis at PA 10°, suggesting an axisymmetric density structure which could act to collimate an outflow along this axis.

In *HST*/WFPC2 imaging observations (Ueta et al. 2000) 17436+5003 appears as an elliptical nebula at optical wavelengths, with a similar extent and orientation to that shown in our NIR data. The object was just resolved in 10.5- and 12.5-μm observations by Skinner et al. (1994) whose deconvolution revealed a dusty torus oriented perpendicular to the major axis of the optical (Ueta et al. 2000) and NIR (this paper) emission. They estimated an inner radius of 0.48 arcsec for this torus. This agrees remarkably well with the 0.6 ± 0.2 arcsec inner radius of the shell seen in the polarized flux images in Fig. 3. It seems highly likely, therefore, that the dust 'torus' seen in emission by Skinner et al. is also responsible for scattering much of the light in our *J*- and *K*-band data, and represents an optically thin, ellipsoidal shell of dust with an equatorial density enhancement. An optically thin nature is required to explain the lack of wavelength effects between the *J* and *K* bands in the polarization data, and also the fact that the optical (WFPC2) data are morphologically very similar to our NIR data. The sharpness of the inner edge of the shell in Fig. 3 indicates that it is physically detached from the star, and that the interior is relatively empty of dust. This is consistent with the Class IVb SED of 17436+5003 (van der Veen, Habing & Geballe 1989; Ueta et al. 2000).

### 3.2.4 IRAS 18095+2704

Observations of 18095+2704 are presented in Fig. 4. In both *J* and *K* total flux the object appears as a bright point source with the telescope diffraction spikes visible. The polarization maps indicate that scattering is indeed occurring, and that 18095+2704 has an extended envelope forming a reflection nebula at NIR wavelengths. In the *J* band the polarization vectors appear aligned preferentially along an axis at PA 23° rather than in a centrosymmetric arrangement, which is indicative of multiple scattering in an axisymmetric or bipolar geometry. A similar pattern is seen at K, although the low signal-to-noise ratio in the scattered component precludes a detailed analysis of the pattern. The low polarization in this object (Table 2) is probably mostly due to the diluting effect of the unpolarized light from the bright star itself; however, the degree of polarization in the wings of the PSF is still only 2.4 per cent maximum. This compares with polarizations of 20 per cent in 17436+5003, a similarly bright and point source-like object, which suggests that the scattering region in 18095+2704 is more compact than in 17436+5003 and therefore more strongly influenced by the stellar PSF. In addition, if a bipolar geometry is advocated, then the low degrees of polarization could be due to a high inclination of the bipolar axis to the plane of the sky.

The polarized flux images shown in Fig. 4 reveal a bipolar geometry for the scattered light in 18095+2704. The orientation of the bipolar axis is at PA 115°, perpendicular to the preferential orientation of the polarization vectors. In both wavebands the brightest point of the polarized flux image is offset to the SE relative to the peak of the total-flux image, which gives the position of the star, so that the SE lobe of the bipolar is larger than

the NW lobe. This also suggests that the bipolar axis is inclined to the plane of the sky, and that the SE lobe is oriented towards us.

This interpretation is supported by the WFPC2 *V*- and *I*-band images of Ueta et al. (2000), which show a bipolar nebula oriented at a similar position angle to that in our polarized flux images, and in which the SE lobe appears the larger and brighter of the two. These authors also comment on the brightness of the central star, and in their classification of this object they suggest that the star is seen directly. This contrasts with the clear bipolar nature of the object in scattered light, indicating that there must be a dusty disc or torus surrounding the star that is responsible for collimating the outflow into two bipolar lobes. The aligned vectors in the polarization patterns at *J* and *K* indicate that dust grains in the bipolar lobes do not have a direct view of the source and that multiple scattering is important. If the optical depth within the scattering region is greater than one in the NIR, then it seems unlikely that we are seeing the star directly in the *V* and *I* bands. However, the star does appear very bright and point source-like, although our *J*-band data show evidence for elongation in the core along the bipolar axis. If this axis is highly inclined to the plane of the sky, then it is possible that we have a preferential view of the star, and that our line of sight lies within the illumination cone of the SE lobe. Trammell, Dinerstein & Goodrich (1994) measure a polarization of 4.5 per cent at 750 nm, rising to 8.5 per cent at 480 nm, for this object, which also indicates that the star is more obscured at shorter wavelengths.

### 3.2.5 IRAS 18184−1623

Observations of 18184−1623 in the *J* band are shown in Fig. 5. There is evidence for an elongation in the core to the SW of the stellar centroid. Due to the brightness of this target and the fast readout mode (Table 1) it is possible that spurious effects may
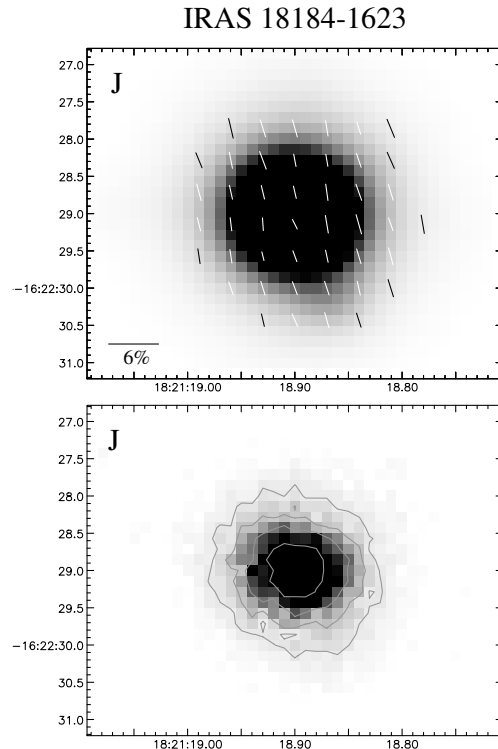


**Figure 5.** Polarimetric observations of IRAS 18184−1623 in the *J* band. Details are as for Fig. 2.

have been introduced. However, observations of a PSF standard star, taken just after $18184-1623$ in the same mode, have a similar FWHM to the target object but show no evidence of elongation. We conclude that the elongation in the core is therefore real.

The polarization pattern is also unusual, consisting of almost parallel vectors oriented at a PA of approximately 20°. Since a total of 72 exposures of $18184-1623$ were taken, we examined subsets of the data for consistency. The polarization pattern was found to be robust within our data set, and not due to a few anomalous exposures. The parallel orientation of the vectors

would normally signify scattering in a very optically thick geometry, such as a dense dusty torus around the star. However, such an axisymmetric scattering scenario would be expected to produce a bipolar geometry in polarized flux which is not seen. The polarized flux image shown in Fig. 5 is point-like and coincident with the peak in total flux. It is possible that we simply have not resolved the bipolar structure. We note, though, that there is slight evidence for an extension of the polarized flux contours to the SW matching the previously noted extension in the total flux.

At MIR wavelengths most of the flux comes from an extended ($12 \times 16\,\text{arcsec}^2$) elliptical nebula with two well-defined peaks
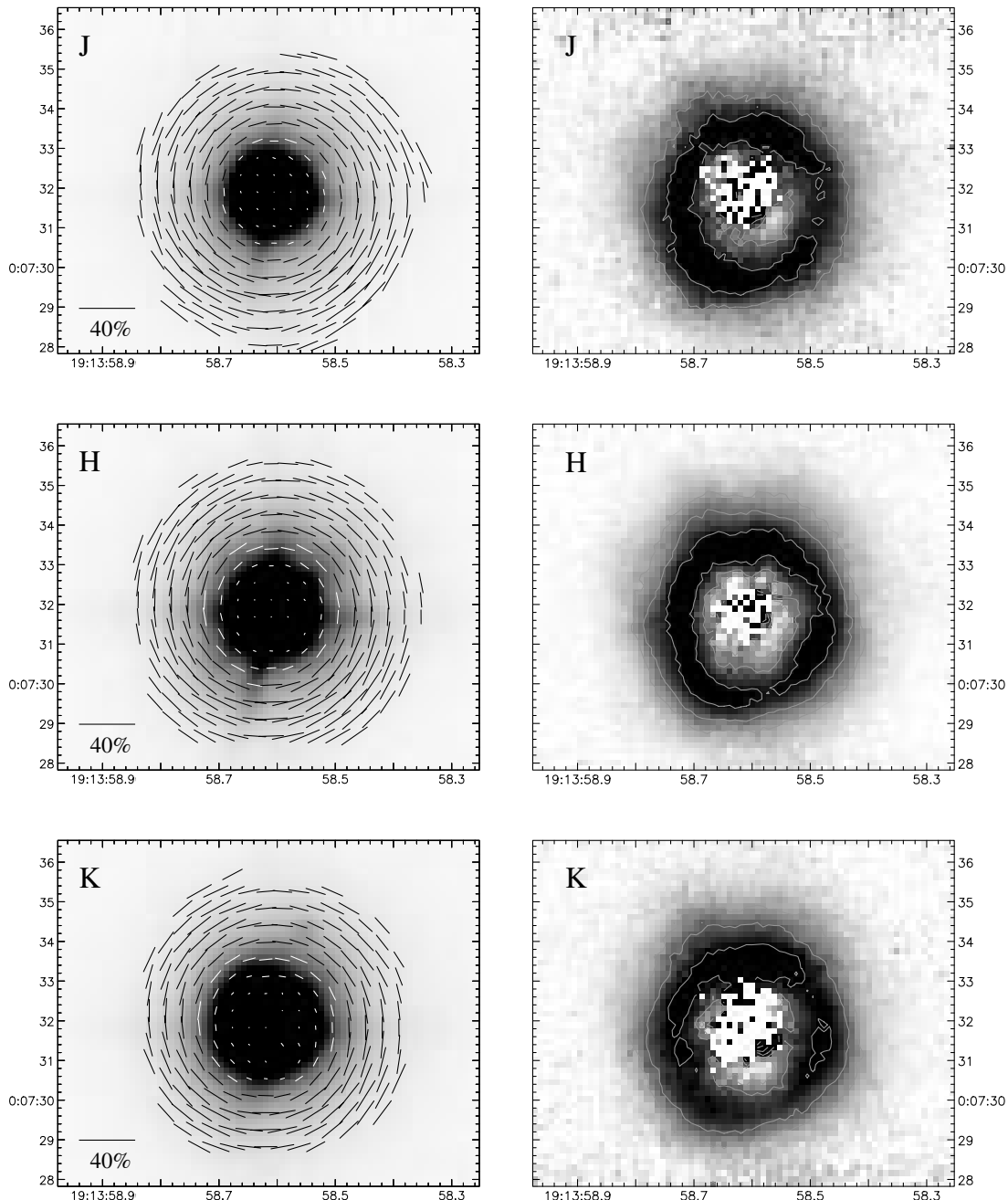
## IRAS 19114+0002



**Figure 6.** Polarimetric observations of IRAS 19114+0002 in the *J*, *H* and *K* bands. The polarized flux contours are spaced logarithmically at intervals of 0.5 mag. Other details are as for Fig. 1, with the addition of the *H*-band observations.

(Robberto & Herbst 1998). These authors suggest that the emission results from 'a relatively thin edge-brightened shell'. A similar morphology is seen by Meixner et al. (1999). Interestingly, the axis of this elliptical dust shell lies at PA 114° (measured from Robberto & Herbst's 10.1-μm image) which is approximately perpendicular to the vector orientation in our polarization map. If the parallel orientation of the vectors is indicative of scattering in an optically thick dust torus, then the polar axis of the torus would lie parallel to the major axis of the extended MIR nebula.

### 3.2.6 IRAS 19114+0002

Observations of 19114+0002 in the *J*, *H* and *K* bands are shown in Fig. 6. The bright, point source-like nature in total flux is evident in all three wavebands (see Table 1). The extent of the image in total flux (defined by a contour at $5\sigma_{sky}$) is 50 pixels (7.2 arcsec) in all three bands.

The polarization maps shown in Fig. 6 show that the star illuminates an extensive reflection nebula. Polarization is reliably detected out to the full extent of the total-flux image. The vector pattern is centrosymmetric to a high degree in all three wavebands, which suggests that the nebula is illuminated isotropically; on the basis of the polarization pattern there is no obvious evidence for axisymmetry. Although the direct light from the star reduces the degrees of polarization in the core region to very low values, the polarizations in the extended nebula are high (Table 2). These values will still be contaminated to some degree by unpolarized light in the wings of the stellar PSF, and to recover the true degree of polarization and its radial dependence the PSF will need to be removed (effectively forming the total-flux image of the scattering nebula). However, the similarity of degree of polarization in the three infrared bands suggests that there are no strong wavelength effects at play as far as scattering is concerned, and that the envelope is, therefore, optically thin.

The polarized flux images show that most of the scattered light originates from a ring of dust surrounding the star. The width of the ring, determined by taking a radial profile in polarized flux and estimating the FWHM, varies between 0.8 and 1.3 arcsec in all three bands. The inner radius varies between 1.1 and 1.6 arcsec, and the outer radius extends to 2.3 arcsec. This brighter structure is then embedded within a more extensive and fainter halo of scattered light which is traced out to a radius of ~4.5 arcsec in our images. The central regions of our polarized flux image are contaminated by residuals due to errors in the registration, normalization and subtraction of the bright core-dominated images, although steps have been taken during the reduction stages to minimize this. However, sufficient information is recorded interior to the bright ring to reveal that polarized flux above the background, and hence dust, is present in this region, and that it is scattering light. In particular, the polarization vector patterns extend inwards beyond the inner boundary of the bright ring and retain their centrosymmetric structure.

The morphology of the ring, as revealed by the polarized flux distribution, is not entirely symmetric, and there are subtle differences between the three wavebands. In particular, the ring thickness varies with azimuthal angle and appears thinnest to the SW at a PA of approximately 195°. This 'thinning' increases with wavelength until in the *K* band it becomes almost a gap in the ring. In the *K* band the ring structure appears more clumpy with the northern portion of the ring the brightest. The stellar centroid is

not located at the centre of the ring, but is instead displaced about 2 pixels (~0.3 arcsec) to the NE. This displacement was also noted by Jura & Werner (1999) in their MIR images.

Coronographic imaging polarimetry of 19114+0002 was obtained by Kastner & Weintraub (1995), who detected the extended scattering nebula out to a radius of 9 arcsec at *J* and 6 arcsec at *K*. This suggests that the dust halo is at least twice as large as shown in our non-coronographic *J*-band images. At a radius of 5 arcsec they measure polarizations of 13 per cent at *J* and 6 per cent at *K*. A radius of 5 arcsec corresponds to the outermost part of the envelope in our detection, where the polarizations are largest. Here we measure polarizations of greater than 25 per cent in both *J* and *K*. We cannot account for the discrepancy, since any correction for the underlying stellar PSF in our data would only serve to increase the degree of polarization. Hawkins et al. (1995) present MIR imaging of 19114+0002 in which their deconvolved 12.5-μm image shows a dust ring encircling the star. This ring, seen in thermal emission, is remarkably similar in both size and morphology to the ring of scattered flux seen in our data, and they undoubtedly arise from the same physical structure. The image of Hawkins et al. (1995) also shows the 'thinning' of the ring to the SW of the star seen in our data. In the WFPC2 survey of Ueta et al. (2000), 19114+0002 appears as an extended nebula with a complex structure of concentric shells forming a rosette. The extent of the nebula in these optical images is similar to that of out NIR images, being approximately 8 arcsec in diameter. They also show clear evidence for a bipolar 'protruberance' at PA 20°, which appears to extend beyond the boundary of the nebula. The SW part of this feature is coincident with the thin part of the dust ring seen in our data and in the MIR image of Hawkins et al. (1995), and may be due to a more recent and more highly collimated outflow breaking out through the dust ring. This is also consistent with our observation that the ring is extended to the SW so that the star no longer resides at its centre.

The high quality of our polarimetric results in three infrared wavebands will allow us to construct detailed scattering models to analyse the structure of the circumstellar envelope in 19114+0002 and these will be presented in a subsequent paper.

### 3.2.7 IRAS 19454+2920

This is the only source in our sample which shows no evidence of polarization. It has been classified as a PPN on the basis of its infrared colours. The *IRAS* flux peaks in the 25-μm band, which indicates a dust temperature of 188 K (Volk & Kwok 1989), and its position in the *IRAS* colour–colour diagram is similar to other objects in our sample (e.g., 19500−1709). Our polarized flux images (not shown) show only noise and residuals from image alignment. If the envelope is smaller than ~0.5 arcsec on the sky, then we will not have resolved it. However, if axisymmetry is present in the envelope, then even in an unresolved observation we would expect to observe a net polarization (equivalent to aperture polarimetry). We conclude therefore that the CSE in this case must have an angular size <0.5 arcsec with no significant axisymmetry (i.e., it is optically thin in the NIR and/or illuminated isotropically).

### 3.2.8 IRAS 19475+3119

Our *J*- and *K*-band observations of 19475+3119 are shown in
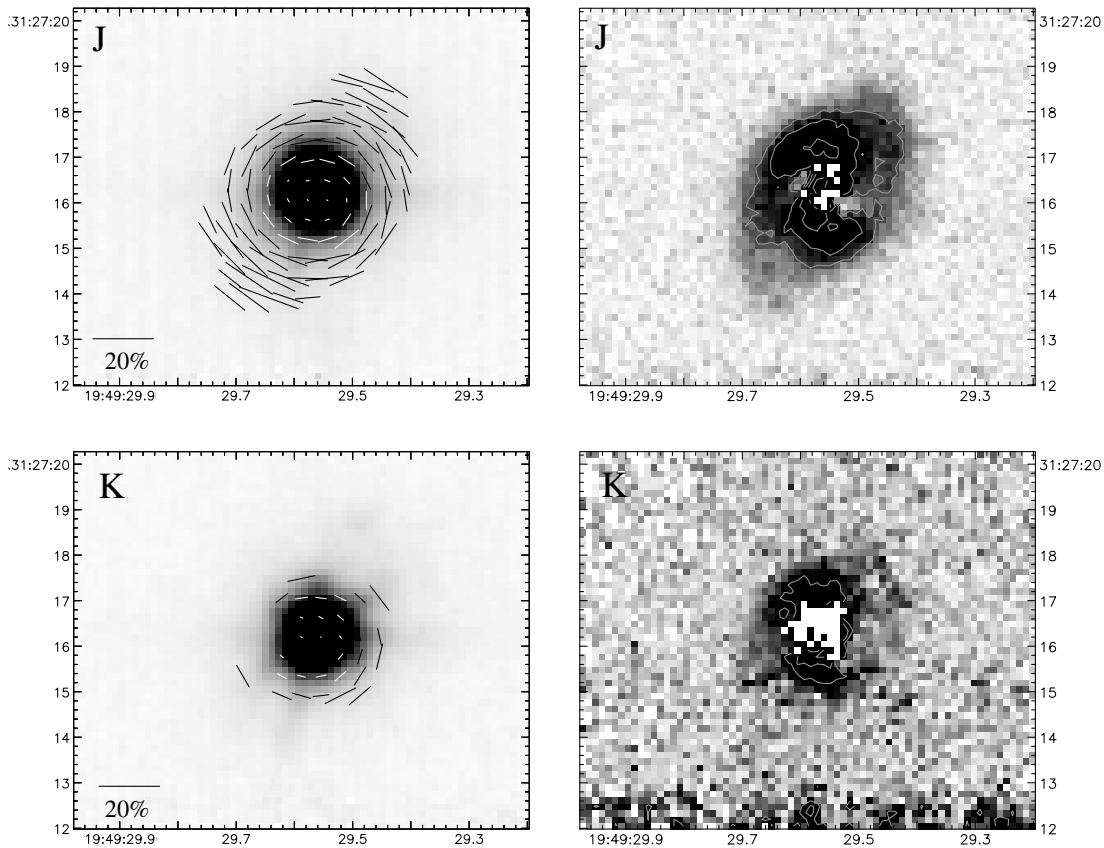
## IRAS 19475+3119



**Figure 7.** Polarimetric observations of IRAS 19475+3119 in the *J* and *K* bands. The polarized flux contours are spaced logarithmically at intervals of 0.5 mag. Other details are as for Fig. 1.

Fig. 7. In total flux the object appears as a bright star with the diameter of the stellar profile (defined using a contour at $5\sigma_{sky}$), being ~5 arcsec at *J*. The intensity contours are similar to those of the PSF star, and show no evidence for deviation from sphericity.

The polarization maps in Fig. 7 show that 19475+3119 does possess an extended scattering envelope. The polarization pattern at *J* is centrosymmetric, indicating that the star is embedded within, and isotropically illuminates, a reflection nebula. The polarizations fall to very low values in the core, suggesting that the star is seen directly and depolarizes the scattered light. The region of scattering is more extended in the SE–NW direction at a PA of 145°, so that the envelope is not spherical. In the *K* band the nebula appears much less extensive, suggesting a lower surface brightness at longer wavelengths, which would be consistent with scattering from dust grains much smaller than the wavelength (Rayleigh scattering, which results in a $\lambda^{-4}$ fall-off in scattering cross-section with increasing wavelength). Nevertheless, a centrosymmetric polarization pattern is still apparent at *K*.

In polarized flux the scattering nebula is clearly elongated in the *J* band data. The fainter emission forms a halo with dimensions of $4.9 \times 3.4$ arcsec$^2$, with the major axis oriented at PA 145°. Superimposed upon this is a remarkable structure which resembles two spiral arms arranged symmetrically about the star. Since the centrosymmetry of the polarization pattern indicates that the illumination of the nebula is isotropic, these structures must represent concentrations of optically thin dust. The dust concentrations are neither parallel nor perpendicular to the long axis of

the nebula, but instead have a rotational point symmetry about the star. In the *K* band, the core of the polarized flux image is contaminated by residuals from the bright stellar PSF, and the faint halo is only barely detected. However, the peaks in polarized flux on either side of the star, seen in the *J* band data, are also seen at *K*.

Previous observations of 19475+3119 have failed to detect evidence of an extended envelope around this source. In their optical imaging observations, Hrivnak et al. (1999a) concluded that there was no evidence for an extended nature. This is not surprising, given the faintness of the scattering halo, the compact nature of the nebula, and the fact that the brightest regions of scattered light are distributed symmetrically about the star. These observations illustrate that imaging polarimetry at high spatial resolution is a very effective technique for detecting and imaging extended scattering envelopes around bright stars. This object is discussed further in Section 4.5.

### 3.2.9   *IRAS 19477+2401*

*J*-band observations of 19477+2401 are shown in Fig. 8. The imaging polarimetry data shown in Fig. 8 indicate that 19477+2401 is clearly extended and is seen in scattered light. Due to the compact nature of this object, we have chosen to display the polarization vectors without any spatial binning, so that each vector represents a measurement in a single pixel. Since
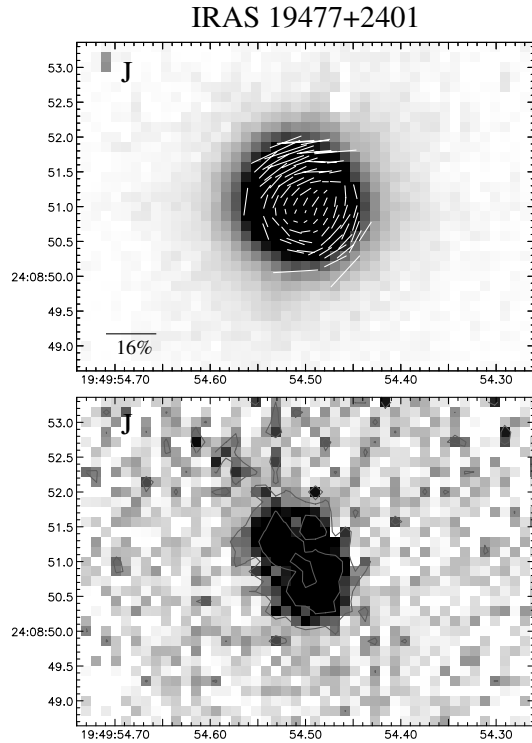
## IRAS 19477+2401



**Figure 8.** Polarimetric observations of IRAS 19477+2401 in the *J* band. Details are as for Fig. 2.

the pixels are smaller than the seeing size (0.143 arcsec compared with a typical seeing disc of 0.5 arcsec), the measurements are not strictly independent. However, a polarization pattern indicative of scattering is clearly seen, with vectors away from the core having a distinct centrosymmetric arrangement. In the core region vectors are aligned at PA ~ 125°, suggesting multiple scattering in an optically thick environment, such as a dusty circumstellar disc.

In *J*-band polarized flux, 19447+2401 appears as a bipolar reflection nebula. Two lobes of nebulosity are visible, separated by a dark lane. The SW lobe appears to be the brighter of the two, and is also the more highly polarized. This suggests that the bipolar axis is inclined to the plane of the sky, and that the SW lobe is oriented towards us. Hrivnak et al. (1999a) noted that 19477+2401 was very faint in their *V*-band data, and was 'extremely red'. This would agree with our interpretation of a star surrounded by an optically thick disc which channels the illumination into two lobes to form a bipolar nebula. Our polarimetry observations suggest that light from the core of this object is multiply scattered so that, despite the stellar appearance in total flux, the star is not seen directly even in the *J* band.

### 3.2.10  IRAS 19500−1709

*J*- and *K*-band observations of 19500−1709 are shown in Fig. 9. In total flux there is no obvious indication of an extension in this object beyond that of the PSF, or of a deviation in the isophotes from those expected of a point source. The polarization maps show that the star illuminates a reflection nebula which extends to a radius of >2 arcsec in the *J* band. Although the polarization
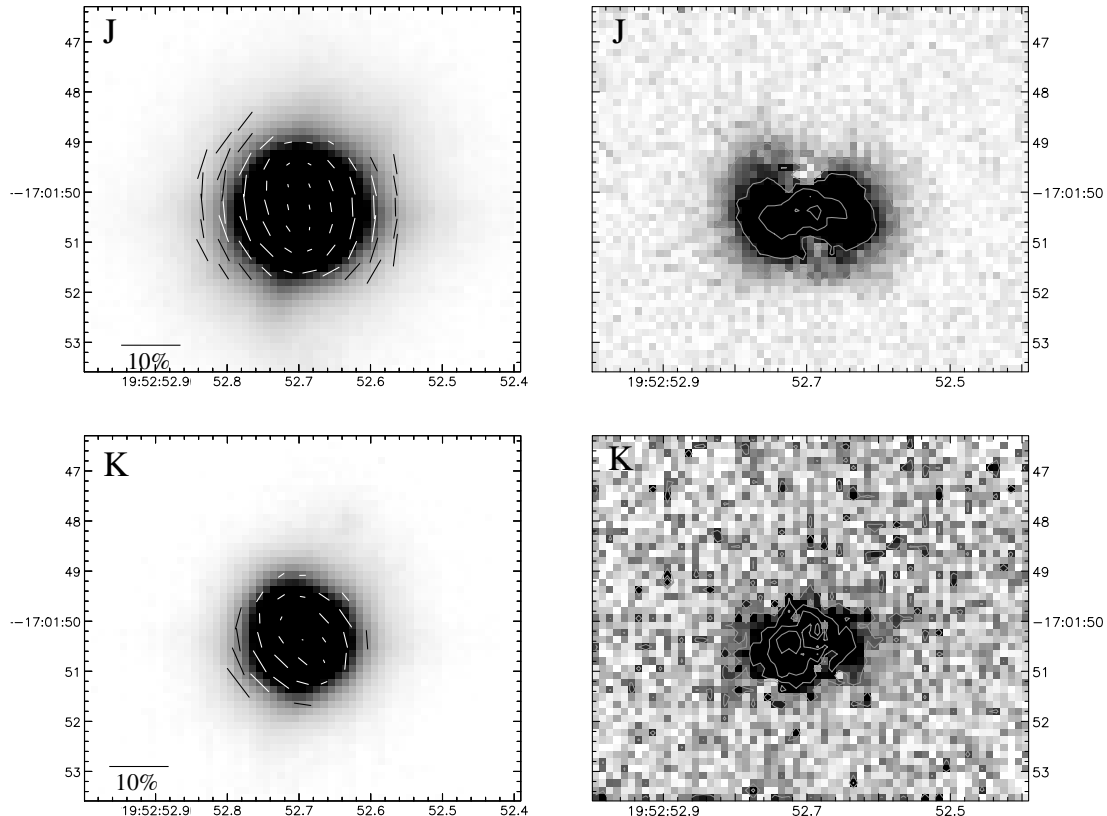
## IRAS 19500-1709



**Figure 9.** Polarimetric observations of IRAS 19500−1709 in the *J* and *K* bands. The polarized flux contours are spaced logarithmically at intervals of 0.8 mag. Other details are as for Fig. 1.
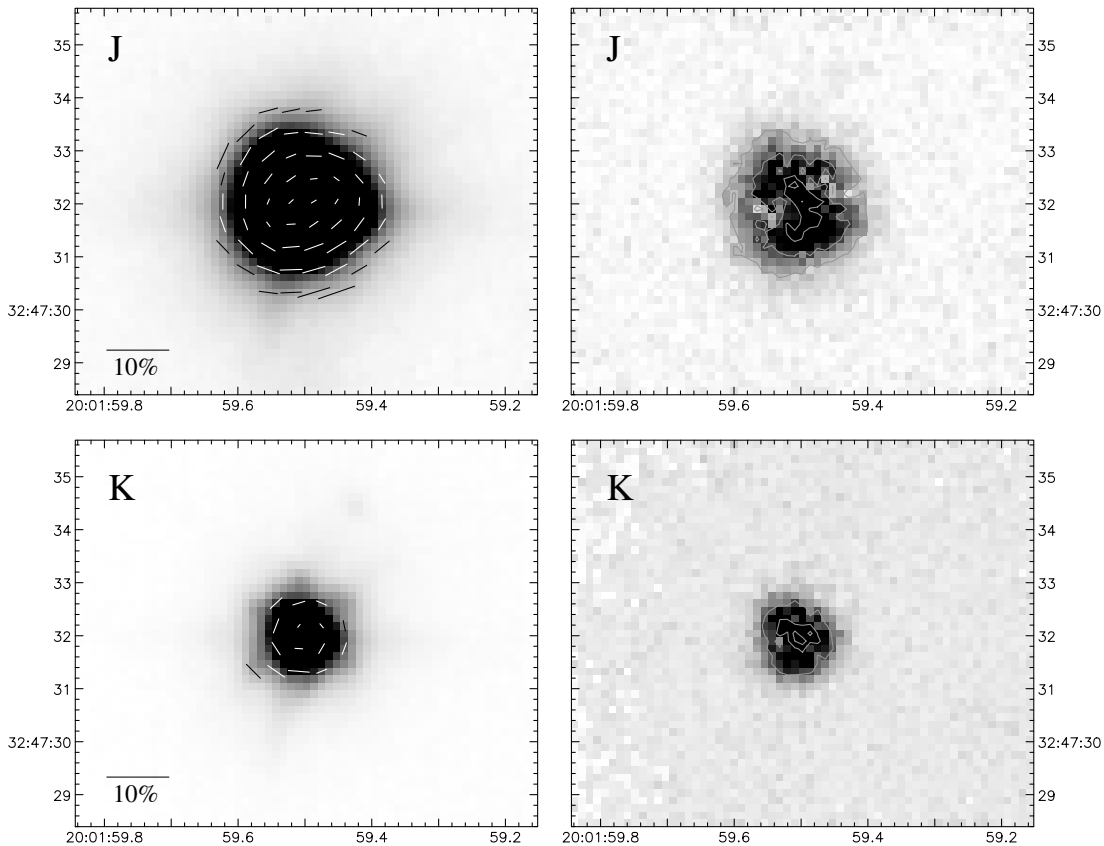
## IRAS 20000+3239



**Figure 10.** Polarimetric observations of IRAS 20000+3239 in the *J* and *K* bands. Details are as for Fig. 1.

pattern appears approximately centrosymmetric, there are deviations which indicate that the illumination is not isotropic. In particular, the polarizations are higher along an E–W axis than along a N–S axis. In addition, there is evidence that the vectors are oriented preferentially N–S in the core region, suggesting that multiple scattering is occurring in this region. The *J*-band polarized flux image clearly shows that the illumination is indeed anisotropic, and that 19500−1709 is a bipolar nebula in scattered light. The major axis of the bipolar, as defined by the brighter regions of polarized flux, is oriented at PA 100°. The two lobes are separated by a dark lane oriented perpendicular to the major axis. This elongated bright structure is superimposed upon a fainter halo which, though less collimated in appearance, is still evidently bipolar. The major axis of the faint halo is oriented more E–W than that of the bright structure, however, suggesting that this object has two axes separated by approximately 10°.

In the *K* band, a similar polarization pattern is seen, although the nebula appears more compact than in the *J* band data. The *K*-band polarization map also shows evidence for anisotropic illumination, and this is confirmed by the polarized flux image which, though noisier than the *J*-band image, is identifiably bipolar. Interestingly, the major axis of the nebula in polarized flux in the *K* band appears rotated by approximately 10° relative to that at *J*. In both the *J* and *K* polarized flux images the E lobe appears brighter, suggesting that the bipolar axis is tilted out of the plane of the sky so that this lobe points towards us.

The existence of an outflow from 19500−1709 is suggested by the detection of a fast ($>40\,\mathrm{km\,s^{-1}}$) velocity component in the

$^{12}$CO $J = 2$–1 and $J = 1$–0 lines (Bujarrabal, Alcolea & Planesas 1992). However, the outflow is not resolved in their data, nor in the $^{12}$CO $J = 2$–1 data of Neri et al. (1998). In optical spectropolarimetry observations, Trammell et al. (1994) did not detect instrinsic polarization in 19500−1709 within their aperture. Our imaging polarimetry observations clearly show that this object is intrinsically polarized and appears as a bipolar reflection nebula in the NIR.

### 3.2.11 IRAS 20000+3239

Observations of 20000+3239 are shown in Fig. 10 for the *J* and *K* bands. The polarization map clearly shows that 20000+3239 has an extended scattering envelope that is illuminated by the central star. The extent of the recorded polarization pattern in the *J* band is 3.5 arcsec in diameter. The vector pattern is approximately centrosymmetric in the outer regions of the nebula, but shows an increasing preference for vector alignment along a PA of 120° closer to the core. The core region is significantly polarized, even with the underlying stellar flux unsubtracted. This suggests that multiple scattering is occurring in the core region, and is consistent with a geometry in which the star is surrounded by an obscuring disc or torus. This then results in anisotropic illumination of the outer regions and the deviation from centrosymmetry in the polarization pattern in these regions. In this interpretation the equatorial plane of the disc/torus would also be at PA 120°. In the *K* band, scattered light is detected, but from a less extended area. The polarization pattern also appears more
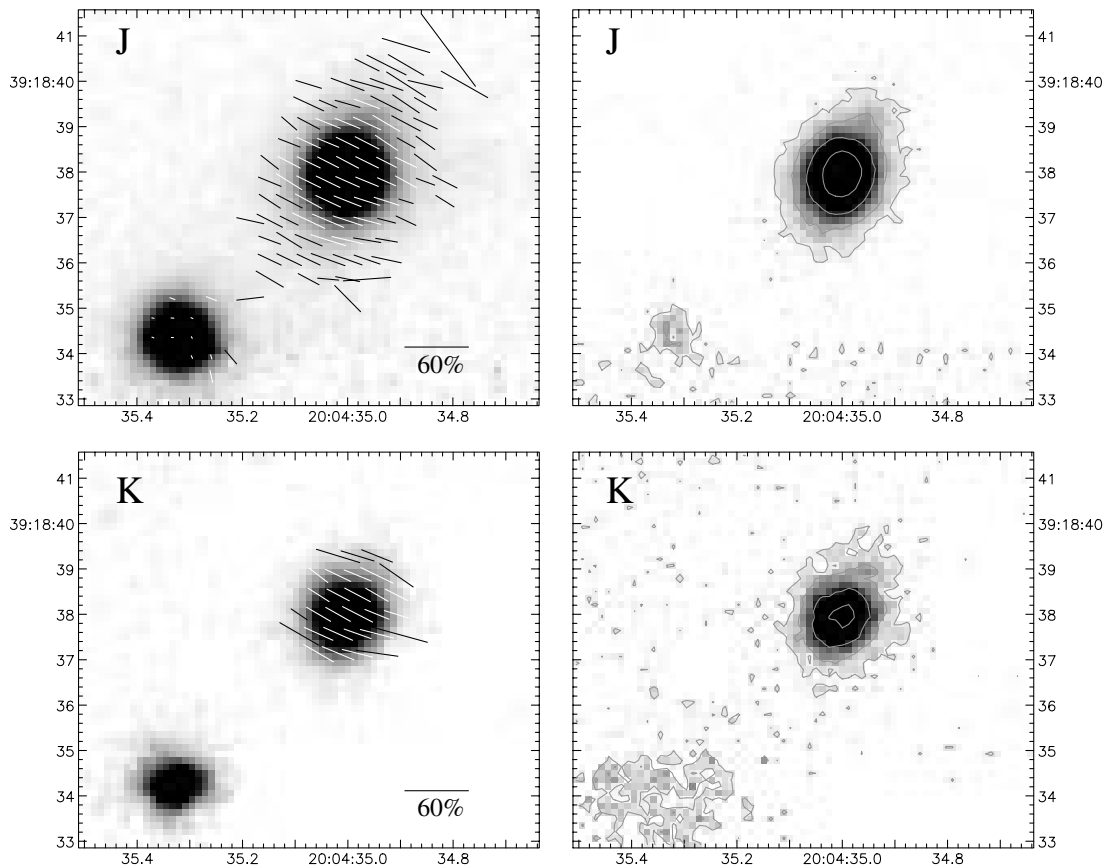
## IRAS 20028+3910



**Figure 11.** Polarimetric observations of IRAS 20028+3910 in the *J* and *K* bands. Details are as for Fig. 1.

centrosymmetric than at *J*, with less evidence for aligned vectors in the core region. This is consistent with scattering in an optically thick dust distribution surrounding the star, which becomes progressively more transparent with increasing wavelength, producing a more centrosymmetric polarization pattern at the longer wavelengths. In polarized flux the scattered light distribution is bipolar. This is particularly evident in the *J* band, where a bipolar structure is seen superimposed upon a fainter and more elliptical halo. The PA of the major axis is 36°, approximately orthogonal to the aligned vector orientation and the postulated circumstellar disc plane. The bipolarity is accentuated by the equatorial 'pinching' in the polarized flux image, which is characteristic of scattering in an axisymmetric geometry. The extent of the faint halo (to a level of $5\sigma_{sky}$ in polarized flux) is 3.7 arcsec along the major axis and 3.3 arcsec perpendicular to it. In the *K* band the bipolar structure is still discernible but obviously more compact. The halo extent in this case is $2.2 \times 1.9$ arcsec$^2$.

This object was observed by Hrivnak et al. (1999a) who, on the basis of their ground-based optical imaging, concluded that it is 'slightly extended' and 'round in shape'. In the MIR imaging survey of Meixner et al. (1999), 20000+3239 appeared 'marginally extended' with a possible E–W elongation. Our polarimetry data clearly shows that this object is both extended and axisymmetric with the star illuminating a bipolar reflection nebula. Given the evidence for multiple scattering in the core region, it is unlikely that the star is seen directly at optical or NIR wavelengths despite its brightness.

### 3.2.12 *IRAS 20028+3910*

Observations of 20028+3910 in the *J* and *K* bands are shown in Fig. 11. The object appears extended and elongated in total flux in the *J* band, especially when compared to the stellar source in the bottom left of the image. The extent of the faint emission, using an isophote at $5\sigma_{sky}$, is $4.0 \times 3.3$ arcsec$^2$, with the major axis at PA 153°. At the highest flux levels, the core is also extended in the same direction, so that 20028+3910 does not have a stellar profile in the NIR.

The polarization maps show a pattern of aligned vectors over most of the object. In both wavebands the vectors in the core region are aligned at PA 65°, orthogonal to the major axis of the object. In the *J* band, there is some evidence for a scattering pattern in the outer regions (with vectors deviating slightly from the aligned pattern), but the polarization map is on the whole typical of scattering in an optically thick environment. The aligned vectors over the source indicate that little or no direct light from the star reaches us, and that the light that we do see is multiply scattered. This suggests a geometry in which the star is surrounded by an optically thick circumstellar torus with equatorial plane at PA 65°, which beams the illumination along its polar axis to form a bipolar reflection nebula. The lack of a centrosymmetric polarization pattern also indicates that dust grains within the nebula do not 'see' the source directly (except perhaps on the bipolar axis). In the *K* band we have detected polarization only in the core region. The polarized flux images show none of the
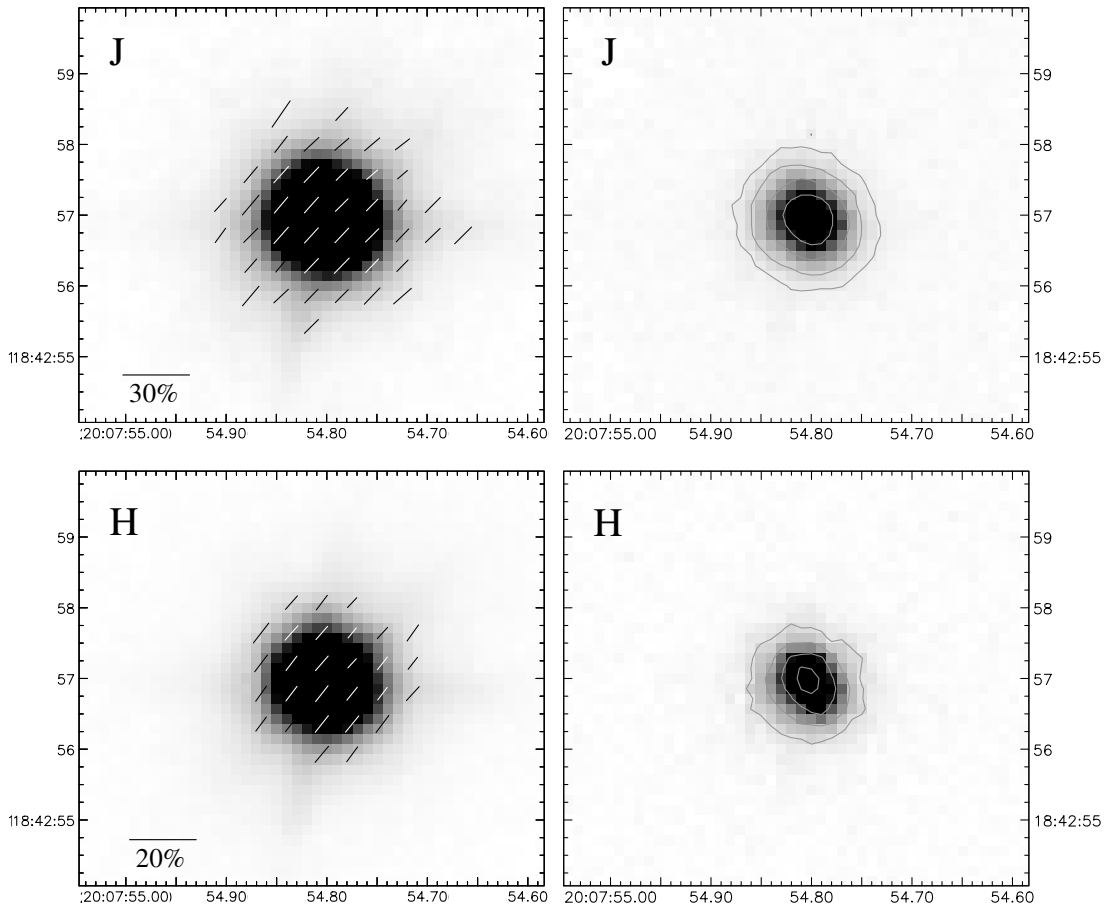
## IRAS 20056+1834



**Figure 12.** Polarimetric observations of IRAS 20056+1834 in the *J* and *H* bands. Details are as for Fig. 1.

features typical of a bipolar nebula. There are no well-defined bipolar lobes nor dark lane across the source. Instead, the polarized flux distribution is centrally peaked and coincident with the peak in total flux. However, the polarization pattern indicates strongly anisotropic illumination of the nebula, which would be expected to result in a bipolar appearance in polarized flux (as is seen, for example, in 17106−3046, 17245−3951 and 19477+2401). There are four other stars in the 20028+3910 field which allow us to reliably estimate the seeing at the time to be 0.82 arcsec (FWHM at *J*). We conclude, then, that although the object has a general elliptical appearance and obvious elongation, the bipolar structure is not clearly revealed in these NIR observations.

Of the four other sources in our ∼1 arcmin square field, two lie within 6 arcsec of 20028+3910, with the closer (bottom left in Fig. 11) at a separation of 3.7 arcsec (PA 134°). It is possible, on the basis of proximity, that this star is associated with 20028+3910, and at a level of $5\sigma_{sky}$ their contours merge in the *J* band. However, there is no evidence that this second object is polarized.

### 3.2.13   IRAS 20056+1834

*J*- and *H*-band observations of 20056+1834 are shown in Fig. 12. In total flux, there is no obvious evidence for extension or elongation, and the polarization maps show a pattern of completely aligned vectors in both wavebands covering the region of the source. In polarized flux, the object appears point source-like at *J* and marginally extended at *H*. The direction of extension at *H* is perpendicular to the vector alignment angle, which suggests that the polarization may be due to scattering in an axisymmetric geometry which is only barely resolved.

Aperture spectropolarimetry of 20056+1834 was obtained by Trammell et al. (1994), who detected a polarization of 4.8 ± 0.1 per cent at PA 21° ± 1° (averaged between 0.5 and 0.7 μm). They find that the PA of the polarization rotates gradually with wavelength, and that the degree of polarization rises into the red. Extrapolation in wavelength of their optical observations to the NIR leads to an estimated degree of polarization of ≈7 per cent at *J* and ≈8.5 per cent at *H*. This is substantially below our measurement of 14.2 per cent at *J*, indicating that the polarization increases faster than a linear extrapolation would suggest. In addition, our observations show that the polarization decreases by a factor of 2 between the *J* and *K* bands.

### 3.2.14   IRAS 21027+5309

Observations of 21027+5309 in the *J* and *K* bands are shown in Fig. 13. In total flux the object appears stellar in both wavebands and has a profile indistinguishable from that of a field star on the same exposure. The polarization maps show a pattern of aligned vectors across the source, and appear very similar to the results
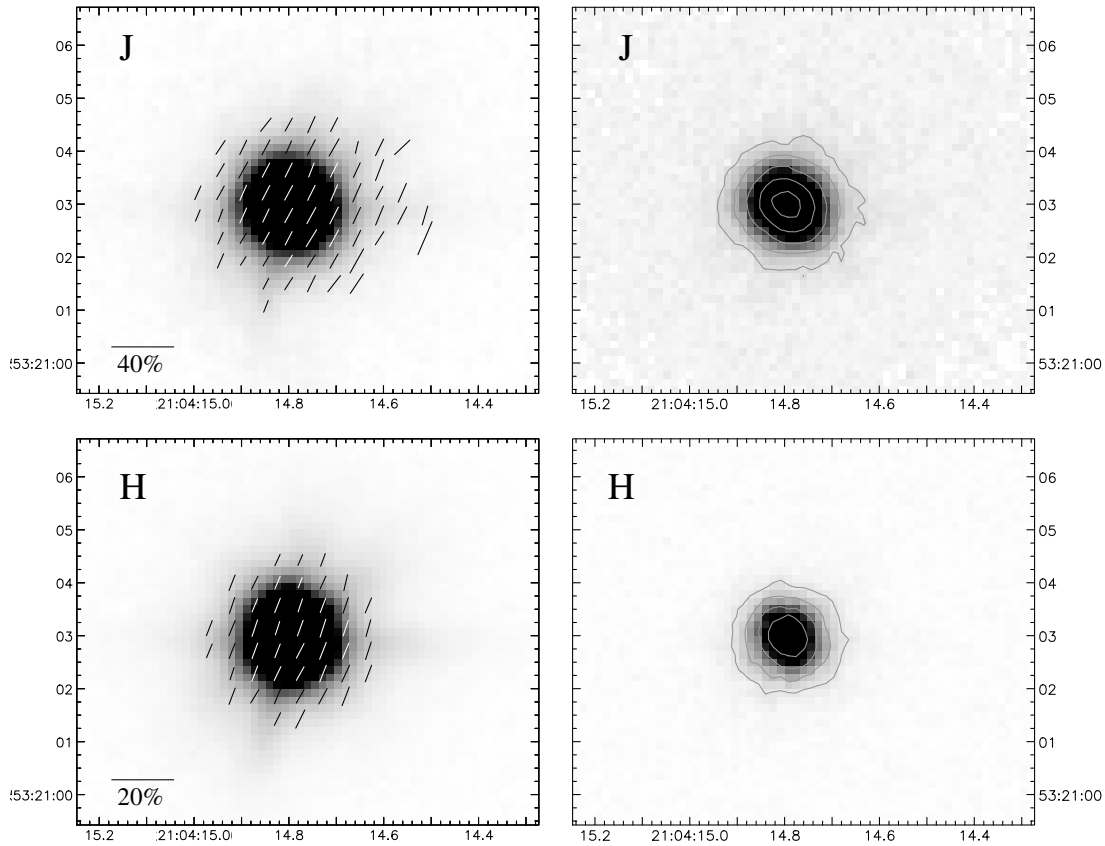
## IRAS 21027+5309



**Figure 13.** Polarimetric observations of IRAS 21027+5309 in *J* and *H* bands. Details are as for Fig. 1.

obtained for 20056+1834. In polarized flux the object is point source-like, with no evidence for elongation or extension in our data. The peak in polarized flux is coincident with the peak in total flux.

Spectropolarimetry of 21027+5309 (=GL 2699) was obtained by Trammell et al. (1994) who measured an average polarization (between 0.5 and 0.7 μm) of 26.49 ± 0.05 per cent at PA 167° ± 1°. This is consistent with an earlier measurement of 27 per cent and 160° by Cohen & Schmidt (1982). The spectropolarimetry shows a steady decline in polarization with increasing wavelength in the optical, which is consistent with our observed polarizations in the *J* and *K* bands. Polarimetrically, this object is very similar to 20056+1834, and both objects will be discussed further in Section 4.2.2.

### 3.2.15 IRAS 22223+4327

Observations of 22223+4327 in the *J* band are shown in Fig. 14. In total flux, the source appears point source-like, with no evidence for extension or elongation. In contrast, the polarization map clearly shows that 22223+4327 has an extended scattering envelope that is illuminated by the central star. The extent of the recorded polarization pattern in the *J* band is 4.5 arcsec in diameter. The vector pattern is approximately centrosymmetric in the outer regions of the nebula, but shows a slight preference for vector alignment along a NE–SW direction. This effect is enhanced by the lower degrees of polarization along this direction

compared with an orthogonal SE–NW axis. The polarization drops to low levels in the core, indicating that it is significantly diluted here by the unpolarized flux from the star itself. However, significant polarization is detected at around the 2 per cent level throughout the core region. A high spatial resolution polarization map (where each vector is a single 0.143 arcsec pixel measurement) is shown in Fig. 14 with the vector length scaled to illustrate the polarization pattern in the core region. The vectors in the core are aligned preferentially along a PA of ≈40°, and form a pattern which is typical of scattering in a bipolar geometry. On either side of the source along this axis (40°) the polarization falls to zero, marking a point where the central aligned vector pattern changes to the centrosymmetric pattern of the outer nebula. At these points the polarization angle rotates by 90°. This effect is often seen in studies of pre-main-sequence stars (e.g. Gledhill 1991), and can result when light is significantly polarized close to the star (due to scattering in a bipolar geometry, for example) before scattering in a more extended envelope.

The polarized flux images of 22223+4327 are particularly interesting. The bipolar morphology responsible for the polarization pattern in the core region can be seen. The major axis of the bipolar nebula is at PA 127°, orthogonal to the vector pattern. Two peaks (lobes) are discernible, offset either side of the stellar centroid. The NW peak appears the brighter of the two, suggesting a tilt out of the plane of the sky with this lobe pointing towards us. The bipolar nebula sits within a ring of polarized flux. The inner and outer radii of this ring are 1.2 ± 0.1 and 2.3 ± 0.1 arcsec respectively.

MIR observations (Meixner et al. 1999) detected resolved emission from 22223+4327 at 12.5 and 18.0 μm (1.9 × 1.7 arcsec$^2$ at PA 108° and 1.9 × 1.8 arcsec$^2$ at PA 152° at 12.5 and 18.0 μm respectively). These results are broadly in agreement with ours if the MIR extension is along the axis of our bipolar. However, it does not appear that the MIR extension corresponds to a detection of the equatorial disc/torus responsible for collimating the bipolar nebula, since this would require a PA in the MIR data of ≈40°. The object is clearly axisymmetric in our NIR data, with the star illuminating a bipolar reflection nebula. This axisymmetry appears to coexist with an approximately spherically symmetric shell which is also seen by reflection.
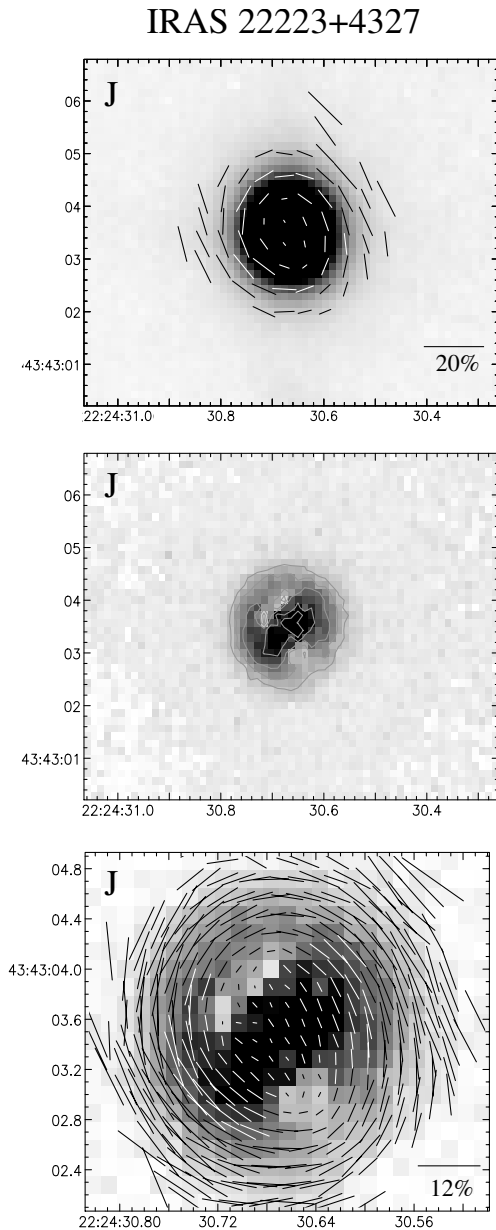


Figure 14. Polarimetric observations of IRAS 22223+4327 in the *J* band. The polarized flux contours are spaced logarithmically at intervals of 0.5 magnitudes. Other details are as for Fig. 2 with the addition of the lower panel showing a higher spatial resolution polarization map (0.14 × 0.14 arcsec bins) superimposed on the polarized flux image.

### 3.2.16  IRAS 22272+5435

*J*-band observations of 22272+5435 are shown in Fig. 15. In total flux the object shows no evidence for extension or elongation. The polarization map is centrosymmetric, indicating that the star illuminates an extended reflection nebula and that the illumination is isotropic. This suggests scattering in an optically thin environment, with little evidence for axisymmetry in the dust distribution. The polarized flux image shows a peculiar distribution of scattered light. A ring-like structure can be seen, with the star located at the centre. The ring appears brighter in the SW portion and much fainter to the north, so that it may be incomplete. The ring is superimposed upon a fainter halo of scattered light which has a distinctive rectangular or box-like shape. We suggest that the polarized flux ring corresponds to a shell of dust around the star, and that this is where most of the scattering is taking place. This shell is part of a more diffuse envelope of dust which forms the fainter halo. As mentioned above, on the basis of the polarimetry there is no evidence for anisotropic illumination, indicating that dust grains in the envelope have a direct view of the star (i.e., it is optically thin). The polarized flux shows that the dust distribution is not isotropic, and the elongation of the faint halo along PA 127° indicates that the envelope expansion is axisymmetric. In this respect 22272+5435 is similar to 17436+5003, another object with an isotropic illumination, a dust shell and an elongated scattering halo. This similarity was also noted by Meixner et al. (1999) on the basis of their MIR data.

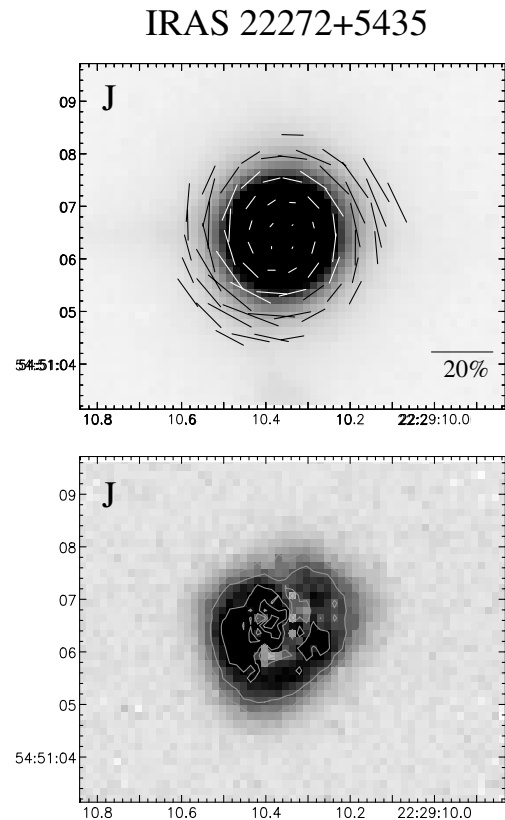In their optical WFPC2 imaging survey, Ueta et al. (2000) note



Figure 15. Polarimetric observations of IRAS 22272+5435 in the *J* band. The polarized flux contours are spaced logarithmically at intervals of 0.5 mag. Other details are as for Fig. 2.

that 22272+5435 has a bright core with four 'elliptical tips'. These elliptical tips appear to result from the superposition of two elliptical nebulae with rotationally offset major axes. The overall effect is to produce an outer edge to the nebula with the box-like geometry we see in the NIR.

### 3.3  Summary of results

Our imaging polarimetry observations of 16 candidate PPNe show that 15 objects have extended CSEs which are seen by scattered light, in the form of NIR reflection nebulae. In direct (unpolarized) light, none of the targets are obviously extended in our 4-m telescope data, and many show no deviation from the PSF measured from nearby calibration stars. It is only in scattered (polarized) light that their extended nature and various morphologies are revealed. We divide the envelope morphologies into three categories, on the basis of their polarization characteristics.

(i) *Shells:* These objects appear shell-like in polarized flux. Most of the scattering is taking place in a shell of dust that is detached from the star. There are five objects in this category: 17436+5003, 19114+0002, 19475+3119, 22223+4327 and 22272+5475. All have centrosymmetric polarization patterns, indicating that the envelope is optically thin and illuminated isotropically by a centrally located point source. The polarization in the core region is very low, as expected for an optically thin shell in which the star is directly visible. The shell is often embedded within a diffuse fainter halo of polarized flux.

(ii) *Bipolars:* These objects are clearly bipolar in polarized flux, with two lobes of nebulosity separated by a fainter region across the 'equator'. Objects in this category are 17106−3046, 17245−3951, 18095+2704, 19477+2401, 19500−1709, 20000+3239 and 22223+4327. The equatorial reduction in polarized flux varies from a slight pinch in the isophotes (e.g., 17245−3951 and 18095+2704) to a dark lane across the central region (e.g., 17106−3046 and 19500−1709). These objects have non-centrosymmetric polarization patterns. We denote the patterns as 'elliptical', in that the vector orientations define the loci of a series of ellipses, rather than a series of circles as in the case of a centrosymmetric pattern. In the extreme case of an 'elliptical' polarization pattern (where the 'ellipticity' becomes very high) the vectors form an 'aligned' pattern. These polarization patterns are typical of scattering in optically thick geometries where multiple scattering occurs close to the source. They are seen frequently in observations of pre-main-sequence stars, and are successfully explained using flattened envelope and disc models (e.g. Lucas & Roche 1998, and references therein).

(iii) *Core-dominated:* These objects have a centrally peaked polarized flux distribution, with the peak coincident with the total flux peak. The polarization patterns are 'aligned', with the vectors being parallel across the source. We find four objects in this class: 18184−1623, 20028+3910, 20056+1834 and 21027+5309. In the case of 18184−1623, 20056+1834 and 21027+5309 the polarized flux distribution appears spherically symmetric and compact, whereas in the case of 20028+3910 it is clearly elongated at low brightness levels forming an elliptical halo.

One object, 22223+4327, features in both the *shell* and *bipolar* categories, and in this respect it is unique within our sample. One object, 19454+2920, appears to be unpolarized. The results are summarized in Table 2.

## 4  DISCUSSION

### 4.1  The prevalence of axisymmetry in PPNe

In Section 3.3 we classified our targets, on the basis of their polarimetric properties, into three categories: *shell*, *bipolar* and *core-dominated* objects. We find six objects in the *bipolar* category, as well as one object (22223+4327) that displays both *shell* and *bipolar* properties. By definition, any object which displays a bipolar structure in polarized flux must be axisymmetric. An indication of the degree of axisymmetry is given by the ratio of the extents of the major and minor axes of the bipolar, and in our data this ranges from 1.1 for 20000+3239 to 2.5 for 19477+2401.

There are four objects in the *shell* category (plus 22223+4327 which is also bipolar and therefore axisymmetric), and three of these are clearly elongated in our data. Both 17436+5003 and 22272+5435 have elongated shells and haloes, and in 19475+3119 the halo is elongated. The axis ratios are 1.6 for 17436+5003, and 1.4 for 19475+3119 and 22272+5435. The fourth object in this category, 19114+0002, is less obviously axisymmetric. Our polarized flux images (Fig. 6) show a ring of dust surrounding the star. Although the ring looks superficially symmetric, there are indications of asymmetries, such as inhomogeneities in the polarized flux around the ring indicating variations in dust density. In particular, there is evidence for a thinning of the ring to the SW, quite apparent in the *K*-band images. Also, the ring is extended slightly to the SW (i.e., it is slightly elliptical), so that the star is not quite at the centre. However, there is no clear *axis* of symmetry demonstrated by these features. WFPC2 imaging observations of 19114+0002 (Ueta et al. 2000) do show evidence for axisymmetry though, especially the striking bipolar 'protruberance' at PA 20°. As mentioned in Section 3.2.6, this structure lines up with the 'gap' in our polarized flux ring. However, there is no evidence to associate the collimation of the bipolar structure with the ring itself. Detailed modelling of this object is currently underway.

In the *core-dominated* category, objects have aligned polarization vector patterns. When accompanied by high degrees of polarization, these indicate multiple scattering in optically thick envelopes with an axisymmetric dust distribution. Similar patterns are seen in nebulae illuminated by deeply embedded pre-main-sequence stars (e.g. Lucas & Roche 1998, and references therein). In both cases (YSOs and PPNe), the axis of symmetry in the dust envelope is perpendicular to the vector orientation. This interpretation is supported when we see elongation in scattered flux along this axis, such as in 20028+3910. Although there is no evidence for elongation in our images of 20056+1834 or 21027+5309, we take their strongly aligned vector patterns and high degrees of polarization to be evidence for axisymmetry in these objects. In the case of 18184−1623, although an aligned pattern is seen, the degree of polarization is comparatively low ($P_J = 2.4 \pm 0.6$ per cent). Such a low degree of polarization could be due to line-of-sight polarization by aligned dust grains in the ISM. However, we note that the direction of alignment is perpendicular to the elongation of the MIR images of 18184−1623 (Robberto & Herbst 1998), again suggesting that it is a manifestation of axisymmetry in this source. These objects are discussed further in the next section.

We conclude that all of our polarized sources (15 out of 16) are illuminating circumstellar envelopes that are to some degree axisymmetric. This is in accord with the surveys of Trammell et al.

(1994) and Ueta et al. (2000), who also found a preference for axisymmetry in PPNe. It is interesting to note that the two objects that show least evidence of axisymmetry in our survey (19114+0002 and 18184−1623) have an anomalous status. Despite sharing some of the characteristics of PPNe, such as a double-peaked SED, it is likely that 18184−1623 is an extremely massive object in the luminous blue variable (LBV) phase, rather than a post-AGB star (Robberto & Herbst 1998). The status of 19114+0002 is still under debate (e.g. Reddy & Hrivnak 1999), with the possibility that this is also a more massive object.

### 4.2    The nature of the core-dominated objects

#### 4.2.1    20028+3910

Observations of 20028+3910 in the *V* and *I* bands with a spatial resolution of ~0.1 arcsec, taken with WFPC2 (Ueta et al. 2000), show a single lobe of nebulosity in the *V* band, offset from the stellar position, with a faint counterlobe emerging in the *I* band. The star is not visible, and appears to be totally obscured in the optical. In addition, the relative brightness of the two lobes suggests an inclination of the bipolar axis to the plane of the sky such that the SE lobe is pointing towards us. Further evidence for bipolarity is seen in the $^{12}$CO measurements of Neri et al. (1998) which show the $J = 1$–0 emission to be extended along the optical bipolar axis and perpendicular to our NIR polarization vectors. In our *J*- and *K*-band data, the dark lane across the star is not seen, and instead of two bipolar lobes we see a centrally peaked distribution of scattered light, coincident with the peak in total flux. However, the aligned polarization pattern across the source suggests scattering in an optically thick environment and that little direct starlight is escaping through the disc in the NIR. Detailed modelling (in progress) is required to determine the optical depth through the disc, but it is likely that the star is only seen in scattered light in the NIR. This is in keeping with the type II/III SED (van der Veen et al. 1989; Ueta et al. 2000). Although no MIR photometry is available, the SED appears to climb uniformly from the NIR to peak at around 25 μm, which is typical of other bipolar nebulae seen close to edge-on, such as 17150−3224, 17441−2411 and 16342−3814. We also have NIR imaging polarimetry data of these three bipolars (in preparation) which (though are more obviously bipolar in appearance than 20028+3910) show the band of aligned vectors across the source. In the case of 20028+3910, the polarization across the source, though high (≈23 per cent), is lower than in the bipolar lobes (≈30 per cent). This is as expected if the source region is viewed mainly by multiply scattered light penetrating the central disc region, whereas in the lobes (which, being on the system axis, have a less obscured view of the source) single scattering is more important resulting in higher polarization and a more centrosymmetric polarization pattern. There is little doubt then that 20028+3910 is a bipolar object. Its core-dominated appearance in the NIR is probably due to an intense region of scattering close to the source.

#### 4.2.2    20056+1834 and 21027+5309

These objects share a number of similarities, which also indicate that they are disparate from the rest of our sample. They were both observed by Trammell et al. (1994), who obtained spectropolarimetry and classified both objects as Type 1c (objects with large intrinsic polarizations where the continua and emission lines have different polarizations). Our observations show aligned vector patterns across the source, and high degrees of polarization that are strongly wavelength-dependent. In both cases the degree of polarization decreases by a factor of 2 or more between *J* and *H* (Table 2).

What is the polarization mechanism in these objects? The lack of any obvious scattering envelope and the uniform polarization angles would be consistent with polarization by dichroic extinction. The interstellar polarization of 1.23 and 1.66 per cent respectively for 20056+1834 and 21027+5309 (Trammell et al. 1994) is much too low to account for the source polarizations, so the polarization must be intrinsic. In a dichroic polarization interpretation, the polarization would occur within an envelope of aligned non-spherical grains around the star. To account for the high degrees of polarization ($P_J \approx 17$ per cent in the case of 21027+5309), grains would need to be coherently aligned throughout much of the CSE. It is possible that this could be achieved by a magnetic field permeating the envelope, but there is as yet little evidence for grain-aligning magnetic fields around post-AGB stars. We note, however, that the fall in polarization by a factor of approximately 2 between the *J* and *H* bands, observed for 20056+1834, is roughly in line with the power-law relationship derived for the dichroic polarization of the ISM in the NIR [$P(\lambda) \propto \lambda^{-1.8}$; e.g. Li & Greenberg 1997].

We favour an interpretation in which the polarization is produced by scattering in an optically thick axisymmetric geometry, as in the case of 20028+3910. In fact, the aligned vector patterns of 20056+1834 and 21027+5309 are just what we see in the core region of 20028+3910. We propose that these two objects are at an earlier evolutionary phase than 20028+3910, and are still in the process of building up a dense equatorial dust disc. Either material has not yet been ejected along the polar axes of these discs, or polar cavities have not yet been excavated so that we do not see a bipolar scattering nebula perpendicular to the disc. When this does happen, we would expect these objects to develop bipolar lobes as in the case of 20028+3910.

It is, of course, possible that both 20056+1834 and 21027+5309 are already bipolars with structure that has not been resolved in our ground-based observations. However, further evidence for an earlier evolutionary status for these objects comes from spectroscopy and photometry, which reveal that both stars are variable. In the case of 20056+1834, the period is 50 d (Menzies & Whitelock 1988). These authors suggest that the star is totally obscured by an optically thick dust cloud, and is seen entirely by reflected light. On the basis of the IR colours, which peak shortward of 10 μm, they fit the dust component of the SED with a 600-K blackbody. This is much hotter than the typically 150–300 K detached dust shells around PPNe, and implies that the dust is much closer to the star. This supports the contention that this object is at an earlier evolutionary phase in which the dust shell has not yet expanded and cooled to PPNe temperatures. 21027+5309 (=GL2699) has been classified by Cohen & Hitchon (1996) as a long-period Mira variable and an extreme carbon star. They derive a period of 1.34 yr, and argue that the strong Hα emission seen in this object results from shocking of a stellar outflow from the inner edge of a circumstellar torus seen almost edge-on. Trammell et al. (1994) also detect strong Hα as well as Hβ, and when Cohen & Schmidt (1982) observed this object, other lines typical of post-shock recombination (such as the forbidden lines of O I, N II and Fe II) were also present. It seems that significant mass-loss is ongoing in 21027+5309, and is probably driven by periodic shocks. This

object may, therefore, still be in the process of building up its circumstellar dust shell.

The fact that both objects show such well-aligned polarization patterns, which we attribute to scattering in an optically thick dusty torus, provides strong evidence that axisymmetry is established before mass-loss terminates at the end of the AGB. In the case of 21027+5309, the ongoing mass-loss is likely to be axisymmetric which may indicate that mass-loss from Miras is generally axisymmetric.

### 4.3 Scattering from superwind shells

Molecular-line studies of AGB stars, particularly CO observations, consistently indicate that the mass-loss rate on the AGB lies between $\sim 10^{-8}$ and $\sim 10^{-5}\,\mathrm{M_\odot\,yr^{-1}}$ (e.g. Loup et al. 1993). These observations cover hundreds of AGB stars, so that the limits seem well established and in particular imply an upper limit to the AGB mass-loss rate not exceeding a few time $10^{-5}\,\mathrm{M_\odot\,yr^{-1}}$. This is 10 times less than the mass-loss rates inferred for well-studied post-AGB objects such as AFGL 618, AFGL 2688 and OH231.8+4.3 (see Bujarrabal 1999, and references therein). Although there is evidence that the mass-loss rate does increase gradually throughout the AGB lifetime of a star (e.g., AFGL 2688; Sahai et al. 1998b) it is hard to escape the conclusion that the AGB must terminate with an abrupt increase in mass-loss, resulting in the ejection of a considerable bulk of material in a short time. This is the *superwind* phase which, on the basis of kinematical arguments, is expected to have a duration $t_{\mathrm{SW}} \sim 10^3$–$10^4\,\mathrm{yr}$ (Kaufl, Renzini & Stanghellini 1993). This dramatic increase in mass-loss over a short period (relative to the AGB lifetime) is expected to result in a *superwind shell* of gas and dust, the inner edge of which marks the cessation of mass-loss and the point at which the star turns off the AGB.

The warm dust at the inner edge of the shell, radiatively heated by the star to $\sim 200\,\mathrm{K}$, will emit at MIR wavelengths. Imaging of four carbon-rich PPNe at 8–13 μm allowed Meixner et al. (1997) to place limits on the size of the superwind shell and, by assuming expansion velocities from molecular-line measurements, on the superwind duration, $t_{\mathrm{SW}}$. For their four PPNe, they find that the inner radii of the shells lie in the range 0.25–1.0 arcsec, with $t_{\mathrm{SW}}$ between 800 and 3000 yr. As long as the dust optical depth is not too high, these shells should also scatter light from the star at optical and NIR wavelengths and, with inner radii of $\sim 1.0$ arcsec, they should be resolvable in our polarimetry data. In fact, we detect shells in five objects (Section 3.3), and it is tempting to identify these structures with superwind shells. In the case of 17436+5003, an elliptical shell is seen in polarized flux, superimposed on a more extended elliptical halo. Although the centre of our image is contaminated with polarized flux residuals resulting from the bright star, the inner edge is well defined (especially in the $J$ band) with a radius of $0.6 \pm 0.2$ arcsec along the minor axis (PA 100°). The thickness of the shell is $1.0 \pm 0.2$ arcsec. The deconvolved MIR images of 17436+5003 (Skinner et al. 1994) indicate a sharp inner radius of the shell of 0.5 arcsec, resulting in two peaks of emission separated by 1.0 arcsec and orientated approximately along the minor axis of our polarized flux image. The correspondence between the MIR and NIR data indicates that they result from the same physical structure, and that we have detected scattering from the superwind shell in 17436+5003. The double-peaked structure seen at 10.5 μm suggests an axisymmetric shell with an equatorial density enhancement along PA 110° (Skinner et al. 1994). This again fits

well with our data which show an elliptical shell with major axis oriented at PA 10° in the 'polar' direction. In the $J$-band image (Fig. 3) the shell appears thinner in the 'polar' regions (along PA 10°) and the fainter halo more extended in this direction, suggesting that the shell is equatorially enhanced and currently focusing the nebula expansion in the polar direction. However, we reiterate that the polarization pattern shows little evidence of deviation from asymmetry so that, even though the dust density is higher at the equator than at the poles, it remains optically thin at 1 μm.

We have also detected shells in four other targets: 19114+0002, 19475+3119, 22223+4327 and 22272+5435. In the case of 22223+4327, the situation is complicated since this object also has a bipolar nebula within the shell. Also, the shell in 19475+3119 has a point-symmetric rather than axisymmetric structure (discussed further in Section 4.5). However, given these differences, our $J$-band data show that the shells are typically less than 1 arcsec in radial width (projected on the sky) which, assuming they result from the superwind, can be used to constrain the duration of this phase. Assuming an actual (rather than sky-projected) angular extent of 1 arcsec, a distance of 1 kpc and a dust expansion velocity of 10 km s$^{-1}$ (a velocity typical of AGB winds; e.g. Loup et al. 1993), $t_{\mathrm{SW}} = 500\,\mathrm{yr}$. This value scales as

$$t_{\mathrm{SW}} = 500 \times \frac{D}{1\,\mathrm{kpc}} \frac{10\,\mathrm{km\,s^{-1}}}{V_{\mathrm{exp}}} \frac{R_{\mathrm{shell}}}{1''}\,\mathrm{yr}.$$

This argument assumes that both the inner and outer edges of the shell are detected in scattered light. For the optically thin cases (centrosymmetric polarization patterns) described here, detection of the inner edge simply depends on whether it can be resolved, whereas detection of the outer edge is a matter of sensitivity in the observations. In a number of our objects we detect a faint outer halo, which gives us some confidence that an outer shell boundary is seen. However, it is not certain that this represents the onset of the superwind outflow, since mass-loss in the early superwind stages may have been lower than at the end and, for an expanding shell, we expect the surface brightness to fall off with radius even if mass-loss is constant over time. Our estimates of $t_{\mathrm{SW}}$ are, therefore, likely to be lower limits. In addition, if the equatorial dust enhancement is sufficient for most scattering to occur in the equatorial region (i.e., in a disc), then inclination effects will be important in calculating the shell thicknesses from the scattered light distribution. Having said this, the main uncertainty in estimating shell properties is, in general, likely to be the distance estimate, which may be uncertain by 200 per cent. We list the observed properties of our shell objects in Table 3, along with estimates of the superwind duration time, $t_{\mathrm{SW}}$, and the dynamical time, $t_{\mathrm{DYN}}$. The latter is determined from the inner radius of the shell, and represents the time since the superwind terminated and during which the shell has been expanding. For the two objects for which estimates of $t_{\mathrm{DYN}}$ are available from MIR measurements (17436+5003 – $t_{\mathrm{DYN}} = 240\,\mathrm{yr}$; Skinner et al. 1994); 22272+5435 – $t_{\mathrm{DYN}} = 1100\,\mathrm{yr}$; Meixner et al. 1997) the agreement with our estimates is remarkably good, again indicating that both the MIR emission and the NIR scattered flux originate from the same dusty shell.

### 4.4 The morphological range of PPNe envelopes

We have identified a range of CSE morphologies in our observations, which we categorize as *core-dominated*, *shell* and

*bipolar* (Section 3.3), and we now discuss the possibility of integrating these morphological types into a common model of a post-AGB CSE. All of our objects show evidence for axisymmetry in the envelope density, and so this must be a key ingredient in any envelope model. It is thought that mass-loss for most of the lifetime of an AGB star is spherically symmetric (e.g. Neri et al. 1998), and that axisymmetry emerges only towards the end of the AGB. This is supported by high spatial resolution (*HST*) observations of the nearby PPN AFGL 2668 (Sahai et al. 1998a,b), which show a pattern of concentric arcs on a background of scattered light with a radial fall-off in surface brightness, indicating that for most of the AGB lifetime the mass-loss has been spherically symmetric with occasional increases in mass-loss rate producing the arcs. This spherically symmetric shell is then illuminated by light which appears to be collimated close to the source in the region of the dark lane forming a highly axisymmetric or bipolar structure. Ueta et al. (2000) suggest that an intrinsically axisymmetric superwind initiates the shift from a spherically symmetric AGB envelope to an axisymmetric envelope by expelling more material in the equatorial region. This forms a superwind shell with a flattened density structure which is able to collimate further outflow and expansion along the polar axes. Ueta et al. also identify two types of object, SOLE (Star-Obvious Low-level Elongated) and DUPLEX (DUst-Prominent Longitudinally Extended) based on the optical depth of the envelopes. In the SOLE objects, the envelope is optically thin and the star is visible at optical and NIR wavelengths. In the DUPLEX objects, the envelope is optically thick and the star obscured. They argue that the two types are physically distinct, and probably result from differing progenitor masses, rather than forming an evolutionary sequence.

This scheme also fits our observations quite well with our *shell* and *bipolar* categories corresponding to the SOLE and DUPLEX categories of Ueta et al. (2000). In the case of the *shell* objects, the superwind shell is optically thin in our NIR data, so that we see scattering throughout the volume of the shell. The low optical depth means that single scattering predominates and a centrosymmetric polarization pattern results. Increasing the optical depth will result in the equatorial regions of the shell becoming opaque in the optical/NIR, so that the scattered light we see originates at higher latitudes, particularly in the polar regions where the dust density is reduced, resulting in a bipolar appearance. The increased optical depth also results in multiple scattering leading to an elliptical or aligned polarization vector pattern rather than a centrosymmetric one. Therefore it is likely that both *shell* and *bipolar* types can be explained with the same envelope model by varying the optical depth, and this will be investigated by detailed modelling.

The *core-dominated* objects, in particular 21027+5309 and 20056+1834, appear to be at an earlier evolutionary phase than the shells and bipolars, as discussed in Section 4.2.2. As the CSEs of these objects expand and start to thin, we may expect them to become more like the bipolar objects as scattered light from the polar cavities becomes visible with decreasing optical depth and as the angular size of the envelope increases. It is not clear, however, that an evolutionary sequence exists between *core-dominated*, *bipolar* and *shell* objects as the envelope evolves and expands and as the optical depth decreases. As pointed out by Ueta et al. (2000), there is little evidence to suggest that the PPNe with optically thin CSEs are older than those with optically thick, disc-like envelopes and bipolar scattering lobes. In particular, there is no obvious trend in the stellar spectral types to indicate this. Therefore we also favour the interpretation that the optical depth of the CSE (and hence the morphological appearance of the PPN) has more to do with the mass outflow rate during the superwind phase than an evolutionary trend.

We do note, however, that the *bipolar* PPNe detected in our survey are consistently smaller in angular extent than the *shell* PPNe (Table 2). Although the distance estimates to these objects are at best uncertain, this may indicate a younger post-AGB status for the bipolars.

## 4.5  Point-symmetric structure

Point-symmetric structure (PSS), that is, structure with a rotational rather than axial symmetry, has been identified in the ionized emission from many PNe. In a sample of 50 PNe, Gonçalves et al. (2000) find that 27 per cent show PSS in emission lines. The origins of PSS are currently under debate, but most models involve some form of rotating or precessing outflow, possibly involving a binary companion (e.g. Frank 2000). The occurrence of PSS in PPNe, seen in scattered light and molecular emission, is less well documented.

We see evidence for PSS structure in just one of our 15 targets with extended CSEs. Fig. 16 shows the *J*-band polarized flux image of 19475+3119. The grey-scale image is superimposed with selected contours, spaced linearly in polarized flux, to

**Table 3.** Observed properties of the shell objects. $R_{in}$ and $R_{sh}$ are the sky-projected inner radii and radial thicknesses of the shells, estimated from our *J*-band polarized flux images. Using the object distance, $D$, and the expansion velocity, $V_{exp}$ (from the literature or assumed), we calculate the duration of the superwind phase, $t_{SW}$ and the time since the superwind terminated (the dynamical time), $t_{DYN}$. The values of $t_{SW}$ and $t_{DYN}$ may be uncertain by up to 200 per cent due to uncertainties in $D$ and other assumptions mentioned in the text.

| Target | $R_{in}('')$ | $R_{sh}('')$ | $D$ (kpc) | $V_{exp}$ (km s$^{-1}$) | $t_{SW}$ (yr) | $t_{DYN}$ (yr) |
|---|---|---|---|---|---|---|
| 17436+5003 | 0.6 ± 0.2 | 1.0 ± 0.3 | 1.2[a] | 12[b] | 500 | 300 |
| 19114+0002 | 2.4 ± 0.3 | 1.4 ± 0.3 | 4[c] | 34[d] | 800 | 1400 |
| 19475+3119 | 0.5 ± 0.2 | 0.7 ± 0.2 | 1† | 10† | 350 | 250 |
| 22223+4327 | 0.6 ± 0.2 | 0.6 ± 0.2 | 1† | 10† | 300 | 300 |
| 22272+5435 | 0.7 ± 0.1 | 0.4 ± 0.1 | 3[c] | 9.6[d] | 650 | 1100 |

[a] Skinner et al. (1994)
[b] Likkel et al. (1991)
[c] Ueta et al. (2000)
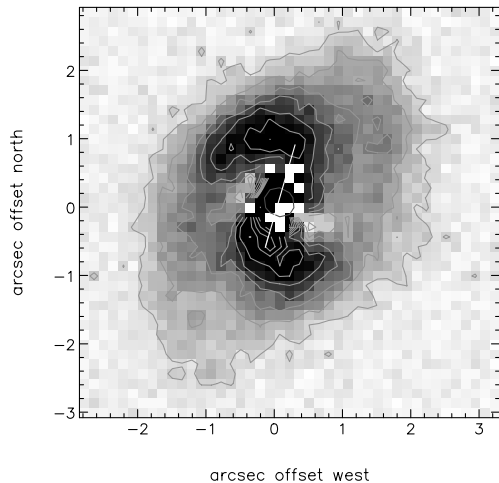[d] Zuckerman, Dyck & Claussen (1986)
† assumed value

**Figure 16.** A close-up view of the CSE of IRAS 19475+3119 seen in scattered light (polarized flux) in the *J* band. Selected contours, spaced linearly, are superimposed on the grey-scale image to highlight the spiral arm structure. The single central contour is at 75 per cent of the total flux peak and marks the position of the stellar centroid. The line drawn between the two polarized flux peaks is 1.4 arcsec in length.

highlight the spiral structure. The stellar centroid is indicated by a single contour in the centre at 75 per cent of the peak intensity. The two 'spiral arms' lie on either side of the star, and curl around for several arcseconds before merging with the faint elliptical halo (see also Fig. 7). We have drawn a line connecting the brightness peaks in the 'arms', and this line passes through the stellar centroid in our data, with the peaks separated by $1.4 \pm 0.1$ arcsec. It is difficult to imagine how a structure with such obvious point symmetry could be accounted for by the 'standard' axisymmetric outflow and envelope models used to explain most PPNe morphologies. Instead, an element of rotation must be introduced. As described in Section 3.2.8, the polarimetry indicates that the dust responsible for scattering is optically thin in the NIR, so we are seeing the illumination of a physical structure.

One way to generate a spiral dust structure would be if an outflow from the star is highly collimated and rotating on a time-scale similar to the outflow time-scale, which in the case of the superwind would be $\sim350$ yr (Table 3). This is a considerable departure from the axisymmetric superwind model which posits that mass-loss is concentrated in a plane, resulting in a shell with a flattened density distribution (e.g. Meixner et al. 1997). An alternative possibility is that we are seeing the disruptive effects of a binary companion on the CSE. The spiral structure bears a remarkable resemblance to the M1 and M2 simulations of Mastrodemos & Morris (1999) in which they treat a binary system in which one component is an AGB star losing mass through a spherical wind. In their model, the spiral structures are accretion wakes, resulting in patterns of density enhancement in the orbital plane of the binary. One obvious constraint from our observations lies in the two-armed structure of the spiral, whereas the simulations of Mastrodemos & Morris show predominantly single spirals winding around the primary. Assuming a distance of 1 kpc to 19475+3119, the separation between the peaks of the spirals is $1.4 \times 10^3$ au, which for the $R_p = 264\,R_\odot$ primary radius assumed in their M1 and M2 simulations, translates as $\sim10^3 R_p$. Hence our spirals are on a much larger scale than the M1 and M2 structures which show spirals out to a radius of $\sim20R_p$. Although we do not have a reliable distance estimate for 19475+3119, our

observations suggest that spiral structure can exist on a size-scale comparable with that of the CSE. Higher spatial resolution images of this object will help to further constrain binary models of AGB mass-loss.

## 5 CONCLUSIONS

In a survey of 16 protoplanetary nebulae (PPNe), principally in the *J* and *K* bands, we detect polarized light and image extended scattering envelopes around 15 objects. The envelopes are typically less than 5 arcsec in extent in our images, although one object (IRAS 19114+0002) is larger (9 arcsec in diameter). In nearly all cases there is evidence for axisymmetry in the dust density distribution, either from the distribution of polarized flux or from the pattern of the polarization vectors (or both). We find a range of morphological types in polarized flux, from *core-dominated* objects to resolved *shells* and *bipolars*. The core-dominated objects have compact scattering envelopes and aligned polarization patterns indicative of scattering in optically thick environments. We argue that these objects may be at an earlier evolutionary phase, so that the CSEs are still dense, compact and close to the star. In one object there is evidence that mass-loss is still ongoing. On the other hand, the shell types are optically thin with centrosymmetric polarization patterns, with the central star visible in the NIR. We find six objects with bipolar morphologies in scattered light, and these generally have 'elliptical' polarization patterns, indicating a higher optical depth than in the shell-type envelopes and a degree of multiple scattering.

We find clear evidence for point-symmetric structure in the CSE of 19475+3119, as seen in scattered light, in both the *J* and *K* bands. The observed spiral structure is similar to the results of simulations involving a mass-losing AGB star with a close binary companion (Mastrodemos & Morris 1999), and so it is likely that this object is a binary.

Apart from 19475+3119, the range of observed morphologies can be explained with a single model of the CSE, in which a shell of dust and gas, with an axisymmetric density distribution, is ejected late in the AGB phase. By varying the optical depth in this 'superwind shell' and the degree to which the dust density is equatorially concentrated, a range of scattered light morphologies will be created. In cases where the dust shell is optically thick in the equatorial plane, scattering in the polar cavities will be enhanced, producing a bipolar morphology. As the optical depth decreases below unity, the shell itself will begin to scatter.

In the five cases where we detect shells in polarized flux, we identify these with the 'superwind shells' and use our imaging observations to place lower limits on the duration of the superwind phase and on the subsequent dynamical time during which the shell has been expanding. These estimates are roughly consistent with those from mid-infrared (MIR) observations, indicating that the scattered and thermally emitted light arises in the same physical structure. We find that the duration of the superwind phase must have been $\sim10^3$ yr.

Starlink Node. Margaret Meixner is thanked for comments that have improved the presentation of the paper.

## REFERENCES

Berry D. S., Gledhill T. M., 1999, Starlink User Note 223, available from http://star-www.rl.ac.uk

Bujarrabal V., 1999, in Le Bertre T., Lèbre A., Waelkens C., eds, Proc IAU Symp. 191, Asymptotic Giant Branch Stars. Astron. Soc. Pac., San Francisco, p. 363

Bujarrabal V., Alcolea J., Planesas P., 1992, A&A, 257, 701

Cohen M., Hitchon K., 1996, AJ, 111, 962

Cohen M., Schmidt G. D., 1982, ApJ, 259, 693

Frank A., 2000, in Kastner J. H., Soker N., Rappaport S., eds, Asymmetrical Planetary Nebulae II, ASP Conf. Ser. Vol. 199. Astron. Soc. Pac., San Francisco, p. 255

Gledhill T. M., 1991, MNRAS, 252, 138

Gonçalves D. R., Corradi R. M. L., Villaver E., Mampaso A., 2000, in Kastner J. H., Soker N., Rappaport S., eds, Asymmetrical Planetary Nebulae II, ASP Conf. Ser. Vol. 199. Astron. Soc. Pac., San Francisco, p. 217

Hawkins G. W., Skinner C. J., Meixner M. M., Jernigan J. G., Arens J. F., Keto E., Graham J. R., 1995, ApJ, 452, 314

Hrivnak B. J., Langill P. P., Su K. Y. L., Kwok S., 1999a, ApJ, 513, 421

Hrivnak B. J., Kwok S., Su K. Y. L., 1999b, ApJ, 524, 849

Jura M., Werner M. W., 1999, ApJ, 525, L113

Kastner J. H., Weintraub D. A., 1995, ApJ, 452, 833

Kaufl H. U., Renzini A., Stanghellini L., 1993, ApJ, 410, 251

Kwok S., 1993, ARA&A, 31, 63

Kwok S., Su K. Y. L., Hrivnak B. J., 1998, ApJ, 501, L117

Li A., Greenberg J. M., 1997, A&A, 323, 566

Likkel L., Forveille T., Omont A., Morris M., 1991, A&A, 246, 153

Loup C., Forveille T., Omont A., Paul J. F., 1993, A&AS, 99, 291

Lucas P. W., Roche P. F., 1998, MNRAS, 299, 699

Mastrodemos N., Morris M., 1999, ApJ, 523, 357

Meixner M., Skinner C. J., Graham J. R., Keto E., Jernigan J. G., Arens J. F., 1997, ApJ, 482, 897

Meixner M. et al., 1999, ApJS, 122, 221

Menzies J. W., Whitelock P. A., 1988, MNRAS, 233, 697

Neri R., Kahane C., Lucas R., Bujarrabal V., Loup C., 1998, A&AS, 130, 1

Reddy B. E., Hrivnak B. J., 1999, AJ, 117, 1834

Robberto M., Herbst T. M., 1998, ApJ, 498, 400

Sahai R., Hines D. C., Kastner J. H., Weintraub D. A., Trauger J. T., Rieke M. J., Thompson R. I., Schneider G., 1998a, ApJ, 492, L163

Sahai R. et al., 1998b, ApJ, 493, 301

Skinner C. J., Meixner M., Hawkins G. W., Keto E., Jernigan J. G., Arens J. F., 1994, ApJ, 423, L135

Su K. Y. L., Volk K., Kwok S., Hrivnak B. J., 1998, ApJ, 508, 744

Trammell S. R., Dinerstein H. L., Goodrich R. W., 1994, AJ, 108, 984

Ueta T., Meixner M., Bobrowsky M., 2000, ApJ, 528, 861

van der Veen W. E. C. J., Habing H. J., Geballe T. R., 1989, A&A, 226, 108

Volk K., Kwok S., 1989, ApJ, 342, 345

Zuckerman B., Dyck H. M., Claussen M. J., 1986, ApJ, 304, 345

This paper has been typeset from a T$_{\rm E}$X/L$^{\rm A}$T$_{\rm E}$X file prepared by the author.